Manuscript submitted to
AIMS' Journals
Volume **X**, Number **0X**, XX **200X**

Website: http://AIMsciences.org
pp. **X–XX**

THE DYNAMICS OF A LOW-ORDER MODEL FOR THE ATLANTIC MULTIDECADAL OSCILLATION

H.W. Broer

Johann Bernoulli Institute for Mathematics and Computer Science, University of Groningen,
PO Box 407, 9700 AK Groningen, The Netherlands

H.A. Dijkstra

Institute for Marine and Atmospheric Research, Utrecht University,
Princetonplein 5, 3584 CC Utrecht, The Netherlands

C. Simó

Departament de Matemàtica Aplicada i Anàlisi, Universitat de Barcelona,
Gran Via 585, 08007 Barcelona, Spain

A.E. Sterk

Johann Bernoulli Institute for Mathematics and Computer Science, University of Groningen,
PO Box 407, 9700 AK Groningen, The Netherlands

R. Vitolo

School of Engineering, Computing and Mathematics, University of Exeter,
North Park Road, Exeter, EX4 4QF, United Kingdom

(Communicated by the associate editor name)

Abstract. Observational and model based studies provide ample evidence for the presence of multidecadal variability in the North Atlantic sea-surface temperature known as the Atlantic Multidecadal Oscillation (AMO). This variability is characterised by a multidecadal time scale, a westward propagation of temperature anomalies, and a phase difference between the anomalous meridional and zonal overturning circulations.

We study the AMO in a low-order model obtained by projecting a model for thermally driven ocean flows onto a 27-dimensional function space. We study bifurcations of attractors by varying the equator-to-pole temperature gradient (ΔT) and a damping parameter (γ).

For $\Delta T = 20^\circ$C and $\gamma = 0$ the low-order model has a stable equilibrium corresponding to a steady ocean flow. By increasing γ to 1 a supercritical Hopf bifurcation gives birth to a periodic attractor with the spatio-temporal signature of the AMO. Through a period doubling cascade this periodic orbit gives birth to Hénon-like strange attractors. Finally, we study the effects of annual modulation by introducing a time-periodic forcing. Then the AMO appears through a Hopf-Neĭmark-Sacker bifurcation. For $\Delta T = 24^\circ$C we detected at least 11 quasi-periodic doublings of the invariant torus. After these doublings we find quasi-periodic Hénon-like strange attractors.

2000 *Mathematics Subject Classification.* Primary: 37N10, 37G35; Secondary: 37C55, 37D45.

Key words and phrases. Atlantic Multidecadal Oscillation, dynamical systems, periodic and quasi-periodic dynamics, bifurcations.

The fourth author is funded by NWO grant ALW 854.00.036.

1. Introduction.

Understanding the dynamics of oceanic low-frequency variability is important for both the development of reliable climate models and the assessment of climate change. In this paper we study multidecadal variability in the North Atlantic sea surface temperature in a low-order model.

1.1. The Atlantic Multidecadal Oscillation.

There is ample observational evidence that the time series of the North Atlantic sea surface temperature (SST) feature a signal of variability with a time scale of several decades.

Observations. From a century of marine observations Kushnir [32] determined the spatial structure of the temperature anomalies: the difference of the SST pattern between the relatively warm years 1970-1980 and the relatively cold years 1950-1964 shows negative anomalies near Newfoundland and positive anomalies in the rest of the basin. Delworth and Mann [17] provide a comparison between simulations of a coupled ocean-atmosphere model and instrumental data supplemented with proxy data. They found an oscillatory mode of variability with an approximate time scale of 70 years.

The name Atlantic Multidecadal Oscillation (hereafter referred to as AMO) for this variability was coined by Kerr [31]. Enfield *et al.* [23] defined an index for the AMO by the 10-year running mean of the detrended Atlantic SST anomalies north of the equator. Figure 1 shows a plot of this index computed from the HadSST2 dataset [1].

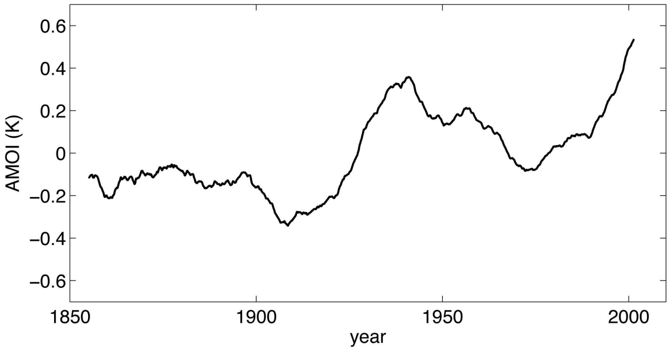

FIGURE 1. Atlantic sea surface temperature anomaly (in K) averaged from 10°N to 90°N and smoothed with a 10-year running mean.

Models and mechanisms. The study of multidecadal oscillations in thermally driven flows in idealised ocean basins goes back to Greatbatch and Zhang [26] and Chen and Ghil [12]. In the latter paper it was suggested that the multidecadal oscillation can be related to the crossing of a critical parameter value. The relation between multidecadal oscillations and Hopf bifurcations was further investigated in the papers of Colin de Verdière and Huck [16], Huck and Vallis [28] and Te Raa and Dijkstra [40].

Te Raa and Dijkstra [40, 41] computed three-dimensional steady flows and their linear stability in a single hemispheric sector basin. By varying a horizontal diffusivity parameter the steady state becomes unstable through a Hopf bifurcation

---

[1] See `http://badc.nerc.ac.uk/data/hadsst2/`.

giving rise to an oscillatory mode with a multidecadal time scale and was named multidecadal mode (hereafter MM). This mode is further characterised by a westward propagation of temperature anomalies and an out-of-phase response between the meridional and zonal overturning flows. This characterisation was used by Te Raa *et al.* [42] to trace the MM through a hierarchy of ocean-only models, and it was found that the MM persists in this hierarchy.

In Dijkstra *et al.* [20], the spatial and temporal characteristics of the MM were traced through a hierarchy of models while monitoring mechanistic indicators, leading to an explanation of the AMO based on changes in the spatial patterns of variability through the model hierarchy. The persistent nature of the MM signature supports the idea that the MM might provide a prototypal explanation for the AMO, see Dijkstra [18, Chapter 6].

Climate variability related to the AMO. The alternating warmer and colder phases of the AMO seem to be correlated with many types of climate variability. For example, Enfield *et al.* [23] found that during warm phases of the AMO most of the United States experience less rainfall, and between warm and cool phases Mississippi River outflow varies by 10%. Goldenberg *et al.* [25] demonstrated that there is a correlation between the warm phases of the AMO and the increase in Atlantic hurricane activity. At present, however, there are no detailed mechanisms known on how the AMO might drive these climate variations.

1.2. **A low-order model for the AMO.**

In this paper we derive a low-order model for the AMO. This means that we aim for a model with the minimum number of ingredients which still captures the phenomenology of the AMO. More specifically:

1. our model only resolves the minimal amount of physics which is necessary to describe the AMO (which is explained below);
2. the governing equations of the model are reduced to a finite-dimensional system of ordinary differential equations.

In a hierarchy of models for the AMO, our low-order model is the simplest possible model. This allows us to give a coherent overview of the dynamics by studying the parameter space and the geometric structure of the attractors in detail.

In this paper we will study how the AMO is amplified by an annual cycle (modelled by parametric forcing). In a forthcoming paper we will consider a low-order ocean-atmosphere model to investigate whether the AMO in its damped regime can be excited by atmospheric variability (possibly through a form of intermittency).

Ingredients of the model. We consider ocean flows in a rectangular ocean basin. These flows are thermally driven by relaxation of the sea surface temperature to an idealised atmospheric temperature gradient. In particular, salinity and wind stress are not taken into account. The governing equations only involve a thermal wind balance (relating vertical shear in the velocity field to horizontal temperature gradients) and an equation for the advection of temperature. These equations are formulated in terms of a system of five partial differential equations together with suitable boundary conditions.

We derive a low-order model by expanding the velocity and temperature field in a truncated series of orthogonal functions and applying a Galerkin projection. This procedure gives a system of 27 ordinary differential equations for the time-dependent expansion coefficients.

Dynamics of the low-order model. The dynamics of the low-order model is investigated using techniques and concepts from dynamical systems. Two parameters are used to study bifurcations of attractors and the associated routes to chaos: ΔT controls the equator-to-pole atmospheric temperature gradient and γ controls the damping of the atmosphere on sea surface temperature anomalies.

First, we study the dynamics of the autonomous low-order model. Next, we apply a periodic forcing modelling annual variations in heat flux at the ocean surface, and we study the associated Poincaré map. In the autonomous low-order model equilibria and periodic attractors are prevalent. The latter bifurcate through (cascades of) period doubling bifurcations, giving rise to Hénon-like strange attractors. The periodic attractors of the autonomous model become invariant tori of the periodically forced system (invariant circles for the Poincaré map) and they bifurcate through quasi-periodic period doubling bifurcations, giving rise to quasi-periodic Hénon-like strange attractors.

Outline of the paper. In Sections 2.1 and 2.2 we formulate the governing equations and describe how the low-order model is obtained. In Section 3.1 we study equilibria and their stability, and in Section 3.2 we study periodic attractors and explain how they are related to the AMO. In Section 3.3 we impose a time-periodic component in the forcing terms and study quasi-periodic attractors by means of a Poincaré map. Section 4 concludes the paper with a discussion of our results.

2. **Model.**

In this section we give a detailed description of the governing equations and sketch the derivation of the low-order model.

2.1. **The governing equations.**

In the present work we use the model of Te Raa and Dijkstra [40] and Dijkstra [19] with the difference that our equations are formulated in Cartesian instead of spherical coordinates. In what follows the coordinates (x, y, z) represent longitude, latitude, and depth, respectively. In addition, we restrict to an f-plane approximation (i.e., the Coriolis force is taken to be constant). According to the mechanism of the multidecadal variability as presented by Te Raa and Dijkstra [40], the AMO is still expected to occur on the f-plane; only the spatial structure of the observed temperature fields and the amplitude of overturning circulations will differ from those obtained from models expressed in spherical coordinates. The ocean length and width of the basin is denoted with L and the depth is denoted with D. The dynamical variables are the velocity field (u^*, v^*, w^*), the pressure field p^*, and the temperature field T^*, where the asterisks indicate that the variable is dimensional.

Forcing. The flows are forced by a restoring heat flux, which means that the heat flux at the surface is proportional to the temperature difference between the sea surface temperature and a prescribed atmospheric temperature T_S^*. As the transfer of heat occurs in a thin boundary layer, which is not resolved in our model, the surface flux forcing is distributed as a body force over a certain depth of the ocean, with thickness H_m using the profile function

$$G(z) = \begin{cases} 1 & \text{if } z \geq -H_m, \\ 0 & \text{otherwise.} \end{cases}$$

Hence, the forcing heat flux is given by

$$Q_{\text{rest}} = \frac{\lambda_T}{\rho_0 C_p H_m}(T_S^* - T^*)G(z), \tag{1}$$

where λ_T (in W m^{-2} K^{-1}) is a constant heat exchange coefficient, ρ_0 is a reference density, and C_p is the specific heat capacity. Observe that the coefficient λ_T is related to a surface adjustment time scale τ_T through the expression

$$\tau_T = \frac{\rho_0 C_p H_m}{\lambda_T}.$$

The prescribed surface temperature of the atmosphere is idealised as

$$T_S^* = T_0 + \frac{\Delta T}{2} \cos(\pi y/L),$$

where T_0 is a reference temperature and ΔT is the equator-to-pole temperature difference.

Governing equations. Temperature differences cause density differences according to

$$\rho = \rho_0(1 - \alpha_T(T^* - T_0)),$$

where α_T is the volumetric expansion coefficient. Moreover, we make the following approximations:

- the effects of density differences are considered only in volume forces, but not in the equations for momentum, temperature and mass conservation (the Boussinesq approximation);
- the vertical pressure gradient balances the buoyancy force (the hydrostatic approximation);
- horizontal and vertical mixing of momentum and heat are represented by constant eddy coefficients (denoted with A_H, A_V, K_H, and K_V, respectively).

We introduce dimensionless variables by using scales L, D, U, and L/U for length, depth, velocity, and time respectively, and we define a rescaled temperature T and non-dimensional pressure p by

$$T^* = T_0 + T, \quad p^* = -\rho_0 g z + f \rho_0 L U p.$$

As the Rossby number $Ro = U/fL$ is small we neglect inertia terms in the momentum equations. Hence, the governing equations for the rescaled variables are given by

$$\begin{aligned}
-v + \frac{\partial p}{\partial x} &= E_H \left(\frac{\partial^2 u}{\partial x^2} + \frac{\partial^2 u}{\partial y^2} \right) + E_V \frac{\partial^2 u}{\partial z^2}, & (2)\\
u + \frac{\partial p}{\partial y} &= E_H \left(\frac{\partial^2 v}{\partial x^2} + \frac{\partial^2 v}{\partial y^2} \right) + E_V \frac{\partial^2 v}{\partial z^2}, & (3)\\
\frac{\partial p}{\partial z} &= Ra\, T, & (4)\\
\frac{\partial u}{\partial x} + \frac{\partial v}{\partial y} + \frac{\partial w}{\partial z} &= 0, & (5)\\
\frac{DT}{dt} &= P_H \left(\frac{\partial^2 T}{\partial x^2} + \frac{\partial^2 T}{\partial y^2} \right) + P_V \frac{\partial^2 T}{\partial z^2} + B(T_S - T)G(z), & (6)
\end{aligned}$$

where

$$\frac{D}{dt} = \frac{\partial}{\partial t} + u\frac{\partial}{\partial x} + v\frac{\partial}{\partial y} + w\frac{\partial}{\partial z}$$

is the advection operator. In the governing equations several nondimensional parameters appear: the horizontal and vertical Ekman numbers E_H and E_V, the Rayleigh number Ra, the inverse horizontal and vertical Péclet numbers P_H and

Parameter	Description	Value	Unit
D	depth of ocean basin	4.0×10^3	m
L	length and width of ocean basin	6.0×10^6	m
U	typical velocity scale	1.0	m s^{-1}
H_m	depth of surface layer	2.5×10^2	m
f	Coriolis parameter	1.4×10^{-4}	s^{-1}
α_T	volumetric expansion coefficient	1.0×10^{-4}	K^{-1}
τ_T	surface adjustment time scale of heat	30	days
ρ_0	reference density	1.0×10^3	kg m^{-3}
C_p	heat capacity	4.2×10^3	J kg^{-1} K^{-1}
A_H	horizontal eddy coefficient of momentum	3.0×10^7	m^2 s^{-1}
A_V	vertical eddy coefficient of momentum	1.0×10^{-3}	m^2 s^{-1}
K_H	horizontal eddy coefficient of heat	1.0×10^3	m^2 s^{-1}
K_V	vertical eddy coefficient of heat	1.0×10^{-2}	m^2 s^{-1}
T_0	reference temperature	15.0	°C
ΔT	equator-to-pole temperature difference	20.0	°C

TABLE 1. Standard values of the dimensional parameters.

P_V, and the Biot number B. These numbers have the following expressions in terms of the dimensional parameters:

$$E_H = \frac{A_H}{L^2 f},\ E_V = \frac{A_V}{D^2 f},\ Ra = \frac{\alpha_T g D}{fLU},\ P_H = \frac{K_H}{LU},\ P_V = \frac{K_V L}{D^2 U},\ B = \frac{L}{\tau_T U}.$$

In what follows, all dimensional parameters have the values listed in Table 1 unless specified otherwise. For the value of the Coriolis parameter f, the high-latitude value at 65°N is taken as being representative.

Boundary conditions. The governing equations are considered on a rectangular ocean basin, see Figure 2. The nondimensional spatial coordinates belong to the domain

$$(x, y, z) \in [0, 1] \times [0, 1] \times [-1, 0],$$

and on the boundaries of this domain we impose the conditions

$$x = 0, 1 \quad : \quad u = v = w = \frac{\partial T}{\partial x} = 0, \tag{7}$$

$$y = 0, 1 \quad : \quad u = v = w = \frac{\partial T}{\partial y} = 0, \tag{8}$$

$$z = -1, 0 \quad : \quad \frac{\partial u}{\partial z} = \frac{\partial v}{\partial z} = w = \frac{\partial T}{\partial z} = 0. \tag{9}$$

Stream function formulation. We obtain a divergence-free velocity field by introducing two scalar velocity potentials ϕ and ψ and setting

$$\begin{pmatrix} u \\ v \\ w \end{pmatrix} = \nabla \times \begin{pmatrix} \phi \\ 0 \\ 0 \end{pmatrix} + \nabla \times \begin{pmatrix} 0 \\ \psi \\ 0 \end{pmatrix} = \left(-\frac{\partial \psi}{\partial z},\ \frac{\partial \phi}{\partial z},\ \frac{\partial \psi}{\partial x} - \frac{\partial \phi}{\partial y} \right)^\top . \tag{10}$$

With this, the continuity equation (5) is eliminated, and the governing equations (2)-(6) can be reduced to a system of four partial differential equations for ϕ, ψ, p, and T. The boundary conditions for ϕ and ψ follow immediately from equations

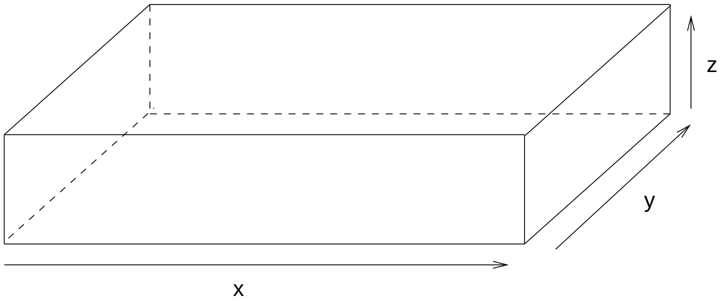

FIGURE 2. Basin of the model: (x, y, z) represent longitude, latitude, and depth, respectively.

(7)-(9). Note that the boundary condition for the vertical velocity w at the top and bottom of the basin leads to

$$\frac{\partial \psi}{\partial x} - \frac{\partial \phi}{\partial y} = 0.$$

The equations for the velocity field (u, v, w) are diagnostic (i.e., they do not contain derivatives with respect to time) and therefore the boundary conditions for the velocity field play a less important role. To simplify the derivation of a low-order model we impose the more strict condition

$$\frac{\partial \phi}{\partial y} = \frac{\partial \psi}{\partial x} = 0$$

to ensure mass conservation.

An advantage of using stream functions is that we can eliminate the pressure gradient in the low-order model since a gradient is orthogonal to a divergence-free field with a vanishing normal component at the boundary (see Appendix A). Hence, the fields ψ, ϕ, and T are the only variables in the low-order model.

2.2. **The low-order model.** The governing equations in (2)-(6) form a dynamical system with an infinite-dimensional state space. We derive a system with a finite-dimensional state space by means of a projection method.

Projection methods. The general idea behind any projection method is to expand the unknown fields T, ψ, and ϕ in terms of a chosen basis, determining the spatial structure, with unknown time-dependent coefficients. An orthogonal projection onto the space spanned by the basis gives a set of finitely many ordinary differential equations for the expansion coefficients.

Examples of a possible basis to project on are empirical orthogonal eigenfunctions, principal interaction patterns (Kwasniok [34]), or eigenvectors computed from a linear stability problem of a particular steady state (Van der Vaart *et al.* [44]). However, these bases have to be computed numerically from a discretised model so that physical parameters must be fixed.

In the present study we use analytical functions for the projection. This choice has the major advantage that physical parameters (e.g., ΔT) are preserved in the projection. Hence, we can do a bifurcation analysis where the bifurcation parameters have a straightforward physical interpretation.

Basis functions. We will use sine and cosine functions with half wave numbers

$$s_m(x) = \sqrt{2}\sin(m\pi x), \quad c_m(x) = \begin{cases} 1 & \text{if } m = 0, \\ \sqrt{2}\cos(m\pi x) & \text{if } m \neq 0, \end{cases}$$

and the functions

$$b_m(x) = \cosh(\lambda_m x) - \cos(\lambda_m x) - \frac{\cosh(\lambda_m) - \cos(\lambda_m)}{\sinh(\lambda_m) - \sin(\lambda_m)}(\sinh(\lambda_m x) - \sin(\lambda_m x)),$$

which are solutions of the boundary eigenvalue problem

$$\begin{cases} \dfrac{d^4 b_m}{dx^4} - \lambda_m^4 b_m = 0, \quad 0 < x < 1, \\ b_m(0) = b'_m(0) = 0, \\ b_m(1) = b'_m(1) = 0, \end{cases}$$

where the numbers λ_m (with $m \geq 1$) are given by the positive roots of the equation

$$\cos(\lambda) = \frac{1}{\cosh(\lambda)}.$$

The Galerkin projection. Denote with

$$R_T = \{(m,n,k) \mid 0 \leq m,n,k \leq 2\},$$
$$R_S = \{(m,n,k) \mid 1 \leq m,n,k \leq 2\},$$

the sets of wave number triplets which are retained in the Galerkin projection. This choice of the retained basis functions gives the smallest possible model in which we still can qualitatively represent the patterns in the temperature and velocity fields which were observed in previous studies of the AMO (see, for example, Te Raa and Dijkstra [40] for pictures of such patterns).

The temperature and velocity potentials are expanded as

$$T(x,y,z,t) = \sum_{(p,q,r)\in R_T} \widehat{T}_{p,q,r}(t)c_p(x)c_q(y)c_r(z),$$
$$\phi(x,y,z,t) = \sum_{(p,q,r)\in R_S} \widehat{\phi}_{p,q,r}(t)b_p(x)b_q(y)s_r(z),$$
$$\psi(x,y,z,t) = \sum_{(p,q,r)\in R_S} \widehat{\psi}_{p,q,r}(t)b_p(x)b_q(y)s_r(z).$$

In this way, the truncated expansions satisfy the boundary conditions. By projecting the equations (2)-(6) onto the basis functions, we obtain a system of 27 ordinary differential equations for $\widehat{T}_{p,q,r}$, and a set of 16 linear algebraic equations to compute the coefficients $\widehat{\psi}_{p,q,r}$ and $\widehat{\phi}_{p,q,r}$. See Appendix A for details.

3. **Results.** We start the investigation of the low-order model by studying equilibria and their stability. For suitable parameter ranges there is a unique equilibrium which loses stability through a supercritical Hopf bifurcation when we increase a certain damping parameter (Section 3.1). The resulting periodic orbit has the spatio-temporal characteristics of the AMO and bifurcates through (cascades) of period doubling bifurcations (Section 3.2).

Finally, we introduce a time-periodic variation in the forcing heat flux (modelling an annual cycle). Then, the Hopf bifurcation of the autonomous system becomes a

Hopf-Neĭmark-Sacker bifurcation, and an invariant 2-torus appears which bifurcates through quasi-periodic period doubling bifurcations (Section 3.3).

The bifurcations of equilibria and periodic orbits discussed in this section are standard, and they are discussed in detail in standard text books on dynamical systems, see, e.g., Broer and Takens [10], Guckenheimer and Holmes [27], or Kuznetsov [33]. For an extensive discussion on quasi-periodic attractors and their bifurcations see Broer *et al.* [2, 1] or Broer and Sevryuk [3].

3.1. **The autonomous system: equilibria.** Throughout this section, state vectors of the low-order model will be denoted by

$$\widehat{T} = (\widehat{T}_{0,0,0}, \widehat{T}_{0,0,1}, \dots, \widehat{T}_{2,2,2}),$$

see Section 2.2 for the meaning of the components. Equilibria of the low-order model will be denoted with $\widehat{T}_{\mathrm{E}}^{(\Delta T)}$, where the superscript emphasizes the dependence upon ΔT.

When the equator-to-pole temperature gradient is set to $\Delta T = 0$°C, the zero vector $\widehat{T}_{\mathrm{E}}^{(0)} = (0, \dots, 0)$ is an equilibrium of the low-order model. This equilibrium corresponds to a motionless ocean with a constant temperature through the entire basin. By continuation we compute an equilibrium $\widehat{T}_{\mathrm{E}}^{(20)}$ for the standard value $\Delta T = 20$°C, and this equilibrium corresponds to a steady ocean flow. In this section we discuss the physical characteristics and the linear stability of such flows.

Physical characteristics. The equilibrium $\widehat{T}_{\mathrm{E}}^{(20)}$ is stable and corresponds to a steady ocean flow, and the corresponding surface heat flux is shown in Figure 3. The sea surface temperature is zonally almost homogeneous. In the northern half of the basin the temperature field is vertically almost homogeneous, whereas in the southern half warmer water masses are located near the surface (Figure 4).

To represent 3-dimensional flows by 2-dimensional plots, we introduce the meridional and zonal overturning stream functions defined by the relations

$$\frac{\partial \Psi_{\mathrm{M}}}{\partial y} = \int_0^1 w(x,y,z)dx, \quad \frac{\partial \Psi_{\mathrm{M}}}{\partial z} = -\int_0^1 v(x,y,z)dx,$$

and

$$\frac{\partial \Psi_{\mathrm{Z}}}{\partial x} = \int_0^1 w(x,y,z)dy, \quad \frac{\partial \Psi_{\mathrm{Z}}}{\partial z} = -\int_0^1 u(x,y,z)dy.$$

The dimensional values of both stream functions are expressed in Sverdrups ($1\,\mathrm{Sv} \equiv 10^6\,\mathrm{m}^3\,\mathrm{s}^{-1}$). The meridional and zonal overturning circulations form single cells (Figure 5). The surface velocity is anticyclonic (i.e., clockwise) and the bottom velocity is cyclonic (i.e., counterclockwise), which is consistent with the unicellular overturnings (Figure 6).

Note that the amplitude of the overturning circulations is relatively large compared to observations. This has several reasons, the most important one being the large value of vertical heat diffusion coefficient K_V. This value has been chosen to prevent unstable stratifications, i.e., cold water on top of warm water. Lower values of K_V can be chosen when a so-called convective adjustment procedure is implemented to prevent unstable stratifications, see Te Raa and Dijkstra [40] for details. Moreover, in the low-order model there is limited spatial resolution. In particular, the ocean basin is too large near the North pole due to the rectangular shape of the basin.

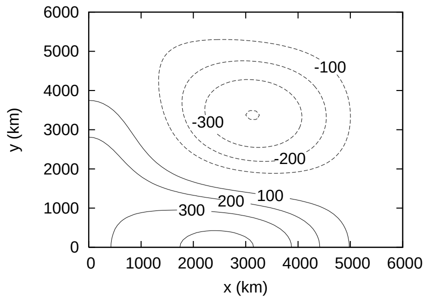

FIGURE 3. Downward heat flux (in W m^{-2}) computed from equilibrium $\widehat{T}_{\rm E}^{(20)}$. Dashed contours denote heat loss to the atmosphere, and solid contours denote heat gain from the atmosphere. Note that the Coriolis force is responsible for breaking the symmetry with respect to the planes $x = 3000$ km and $y = 3000$ km.

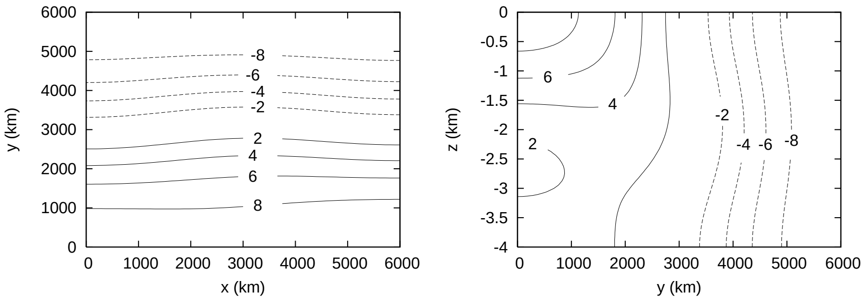

FIGURE 4. Physical characteristics of the steady flow associated with the equilibrium $\widehat{T}_{\rm E}^{(20)}$. Left: non-dimensional sea surface temperature. Right: cross section of the non-dimensional temperature field at $x = 4000$ km. Dashed contours denote negative temperatures, and solid contours denote positive temperatures. Dimensional temperatures are obtained by adding the reference temperature T_0.

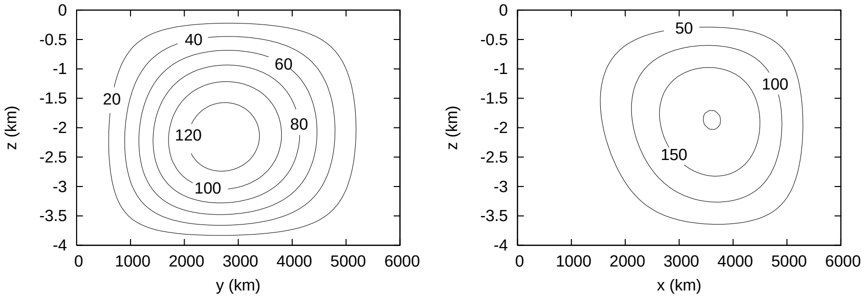

FIGURE 5. Physical characteristics of the steady flow associated with the equilibrium $\widehat{T}_{\rm E}^{(20)}$. Left: meridional overturning circulation (in Sv). Right: zonal overturning circulation (in Sv).

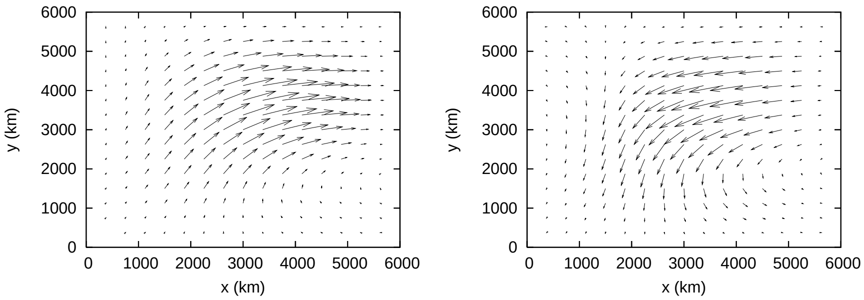

FIGURE 6. Physical characteristics of the steady flow associated with the equilibrium $\widehat{T}_{\mathrm{E}}^{(20)}$. Left: surface velocity. Right: bottom velocity.

Stability under prescribed heat flux. Once we have obtained a stable equilibrium $\widehat{T}_{\mathrm{E}}^{(\Delta T)}$ we define the constant term

$$Q_{\text{pres}} = B(\widehat{T}_S - \widehat{T}_{\mathrm{E}}^{(\Delta T)}),$$

which will be referred to as the prescribed heat flux associated with the equilibrium $\widehat{T}_{\mathrm{E}}^{(\Delta T)}$. Next, we define a new heat flux Q_γ by setting

$$Q_\gamma = (1-\gamma)Q_{\text{rest}} + \gamma Q_{\text{pres}}, \tag{11}$$

where γ is a nondimensional parameter interpolating between restoring and prescribed heat flux conditions. This parameter essentially modifies the atmospheric damping of sea surface temperature anomalies. The choice $\gamma = 0$ corresponds to the damping time scale τ_T (Section 2.1), and when γ increases to 1, this time scale increases to infinity (no damping). Now we replace (1) in the equations by (11). By construction, the equilibrium $\widehat{T}_{\mathrm{E}}^{(\Delta T)}$ remains an equilibrium under the heat flux Q_γ for all values of γ. In this way we can study stability of the equilibrium under the same heat flux, but with a different effect of atmospheric damping on the sea surface temperature.

For the parameter range

$$2 \times 10^7 \leq A_H \leq 1 \times 10^8, \quad 5 \times 10^{-4} \leq K_V \leq 1 \times 10^{-2},$$

the equilibrium $\widehat{T}_{\mathrm{E}}^{(20)}$ is stable for $\gamma = 0$. However, by varying γ from 0 to 1, the equilibrium can become unstable. Figure 7 shows the number of unstable eigenvalues as a function of the parameter A_H for different values of K_V. Clearly, the equilibrium loses stability through a succession of bifurcations. These bifurcations can only be pitchfork, transcritical, or Hopf bifurcations: since the equilibrium $\widehat{T}_{\mathrm{E}}^{(\Delta T)}$ persists for all values of γ, the possibility of saddle-node bifurcations is ruled out.

3.2. **The autonomous system: periodic attractors.**

When we fix the values of A_H and K_V as in Table 1 the steady flows of the previous section only lose stability through a supercritical Hopf bifurcation. The obtained periodic flow is a multidecadal mode of variability with a period of about 50 years which is characterised by a westward propagation of temperature anomalies and a phase lag between the zonal and meridional overturning anomalies. In turn, for values of $\Delta T \geq 22$°C, this mode loses stability through (cascades of) period doubling bifurcations.

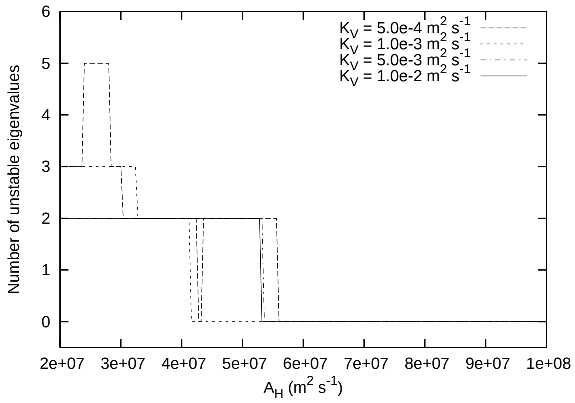

FIGURE 7. Stability of the equilibrium $\widehat{T}_{\mathrm{E}}^{(20)}$ under prescribed heat flux ($\gamma = 1$). The number of eigenvalues with positive real part is plotted as a function of A_H for fixed values of K_V.

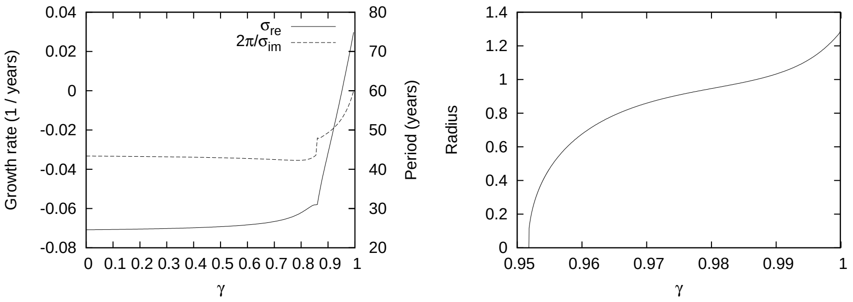

FIGURE 8. The Hopf bifurcation of the equilibrium $\widehat{T}_{\mathrm{E}}^{(20)}$. Left panel: the growth factor (σ_{re}) and period ($2\pi/\sigma_{\mathrm{im}}$) of the least stable eigenvalue pair is plotted as a function of γ for A_H and K_V fixed as in Table 1. A Hopf bifurcation takes place for $\gamma_H \approx 0.951$ where the growth rate becomes positive. Right panel: radius of the periodic attractor as a function of γ.

The Hopf bifurcation. By increasing the parameter γ from 0 to 1 the equilibrium $\widehat{T}_{\mathrm{E}}^{(20)}$ becomes unstable through a supercritical Hopf bifurcation which takes place for $\gamma_H \approx 0.951$ (left panel of Figure 8). Observe that close to the Hopf bifurcation the radius of the periodic orbit is of the order $O(\sqrt{\gamma - \gamma_H})$ as predicted by normal form theory (right panel of Figure 8).

Linearising the vector field around the Hopf bifurcation gives two eigenvalues $\pm\sigma_{\mathrm{im}} i$ on the imaginary axis. Let $\Phi_{\mathrm{re}} \pm i\Phi_{\mathrm{im}}$ denote corresponding eigenvectors. Then

$$P(t) = \cos(\sigma_{\mathrm{im}} t)\,\Phi_{\mathrm{re}} - \sin(\sigma_{\mathrm{im}} t)\,\Phi_{\mathrm{im}} \tag{12}$$

is a periodic orbit of the vector field obtained by linearisation around the equilibrium undergoing the Hopf bifurcation. This periodic orbit can be interpreted as a periodic anomaly imposed on the steady background flow associated with the equilibrium $\widehat{T}_{\mathrm{E}}^{(20)}$. The physical signature of the anomalies can be studied by looking at the patterns associated with the phases $P(-\pi/2\sigma_{\mathrm{im}}) = \Phi_{\mathrm{im}}$ and $P(0) = \Phi_{\mathrm{re}}$. The sea surface temperature associated with the eigenvectors are shown in the top panels of Figure 9. A warm tongue at the sea surface has travelled westward during one quarter of the oscillation. In addition, there is a phase lag between the meridional and zonal overturning flows, see the bottom panel of Figure 9. In summary, these characteristics qualitatively agree with those of the multidecadal mode detected in Te Raa and Dijkstra [40].

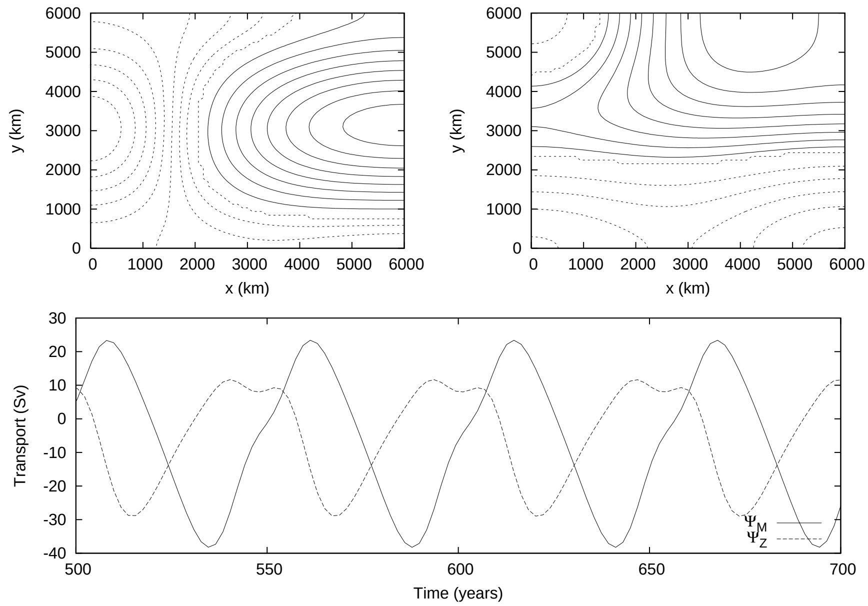

FIGURE 9. Physical characteristics of the periodic anomaly $P(t)$ defined in (12). Top panels: westward propagation of the sea surface temperature anomalies $P(-\pi/2\sigma_{\mathrm{im}})$ (left panel) and $P(0)$ (right panel); contour values are omitted as the scales are arbitrary (any scalar multiple of (12) is also a solution of the linearised system). Bottom panel: basin averaged values of the meridional and zonal overturning circulations; observe the phase difference.

The period doubling bifurcations. For $\Delta T = 20°\mathrm{C}$ the periodic orbit remains stable up to $\gamma = 1$. However, for larger values of ΔT the periodic orbit can bifurcate through one or more period doubling bifurcations.

In Figure 10 we have plotted 1-dimensional projections of attractors of a local Poincaré map defined by the section $\{\widehat{T}_{0,0,1} = 2\}$. For each parameter value 500 iterates of the Poincaré map are computed of which the last 100 points are plotted. Then the parameter γ is increased with 5×10^{-5} and the last computed point is used as initial condition for a new loop. For $\Delta T = 22°\mathrm{C}$ there are only two consecutive period doubling bifurcations, but for larger values we observe a full cascade of period doublings where regions of chaotic behaviour are interrupted with windows of periodic behaviour.

The occurrence of the period doubling bifurcations as indicated in Figure 10 is slightly shifted to larger values of the parameter with respect to the actual location.

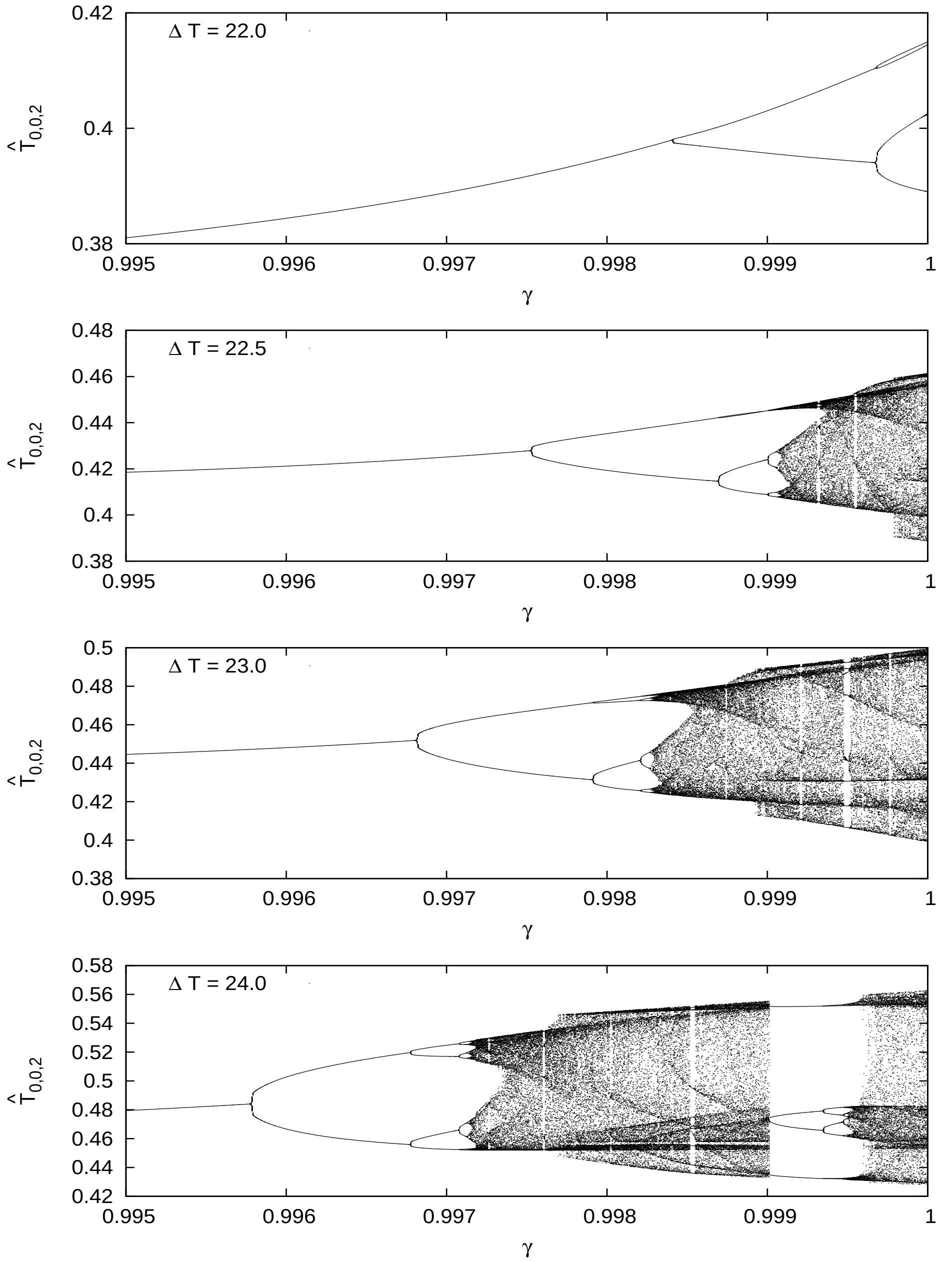

FIGURE 10. Period doubling cascades of the AMO mode in the autonomous system for various values of ΔT, visualised in the Poincaré section $\widehat{T}_{0,0,1} = 2$. The components $\widehat{T}_{0,0,2}$ are plotted as a function of γ. For each parameter value 500 iterates of the Poincaré map are computed and only the last 100 iterates are plotted. Then the parameter γ is increased with 5×10^{-5} and the last computed iterate is used to start a new loop.

This is due to intermittency near the bifurcations: the periodic orbits that are losing stability are only weakly unstable near the bifurcation point. Therefore a large number of iterations (larger than that used in Figure 10) is required to converge to the 'doubled' orbit. This results in tiny 'delays' in the apparent location of the period doubling bifurcations. See Neishtadt *et al.* [35] and references therein for a detailed discussion on bifurcation delay.

At the first period doubling, the periodic orbit associated with the AMO loses stability which gives birth to a new periodic orbit which makes two loops before closing, and which has roughly twice the period of the original periodic orbit. The new periodic orbit inherits the physical characteristics of the AMO (i.e., the phase-lag in the overturning circulations and the westward propagation of temperature anomalies), but the period doubling has introduced a harmonic of approximately 100 years in the variability. At subsequent period doublings more harmonics (200 years, 400 years, 800 years, etc.) are introduced in the power spectrum (not shown).

Hénon-like strange attractors. The left panel Figure 11 shows a strange attractor which appears for $(\Delta T, \gamma) = (24; 0.998)$ after a cascade of period doubling bifurcations of a fixed point of the Poincaré map defined by the section $\{\widehat{T}_{0,0,1} = 2\}$ (see the bottom panel of Figure 10). The right panel of the same figure shows a short piece of the 1-dimensional unstable manifold of an unstable fixed point obtained by continuation of the stable fixed point which is present for $\gamma = 0.995$. This unstable manifold almost coincides with the strange attractor, which suggests that the latter is indeed Hénon-like. Figure 12 is the same as Figure 11, but a different projection has been used. Observe that the unstable manifold is folding in very wild way. This causes the component $\widehat{T}_{0,0,0}$ to seem to behave in a noisy way.

The reader is referred to, e.g., Simó [38] for the methodology of computing invariant manifolds.

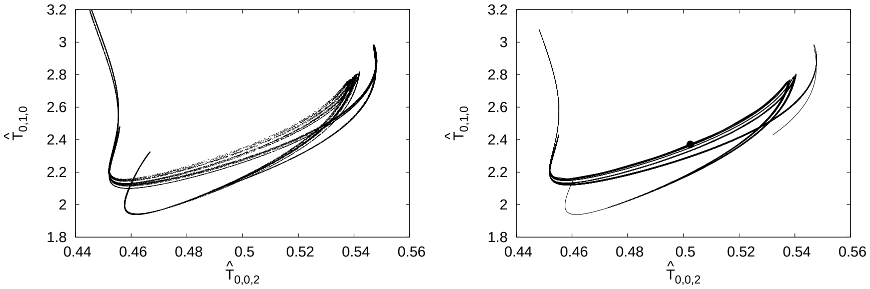

FIGURE 11. Left: strange attractor obtained for $(\Delta T, \gamma) = (24; 0.998)$. Right: the 1-dimensional unstable manifold of the unstable fixed point (marked as a dot on the plot) of the Poincaré map obtained by continuation of the stable fixed point which appears for $\gamma = 0.995$. Note the similarity between this curve and the strange attractor. However, there are differences in the structure of the attractor and the displayed part of the manifold; for a complete agreement one should compute a longer piece of each side of the manifold, counted from the fixed point. This requires more iterations and produces a huge file.

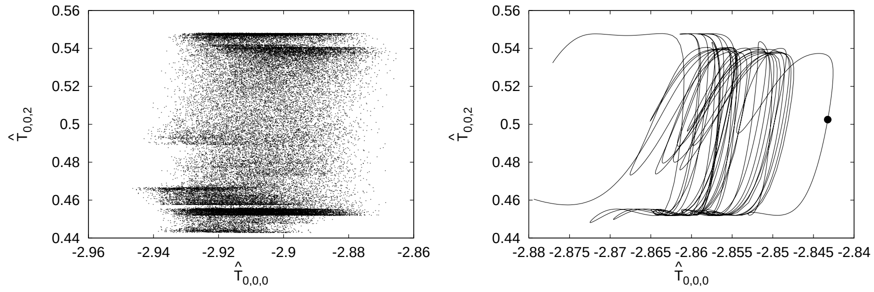

FIGURE 12. Same as in Figure 11, but in a different projection. Observe the wild foldings in the unstable manifold: this causes the 'white noise'-like behaviour in the variable $\widehat{T}_{0,0,0}$.

Attractors for $\gamma > 1$. The parameter γ only has a physical meaning when its value is between 0 and 1, but attractors appearing for $\gamma = 1$ can persist for values $\gamma > 1$. We have used the same algorithm of Figure 10 to extend the computation of the attractors to values $\gamma > 1$ (not shown). The results are sensitive with respect to the choice of initial condition and of the step size $\Delta\gamma$ which is used to increase the parameter γ. Not all initial conditions converge to an attractor: orbits may diverge to infinity, depending on the initial point. Also, when starting from an initial point p on an attractor for some value $\gamma = \gamma_0$, the point p may fall outside the basin of the attractor occurring at $\gamma = \gamma_0 + \Delta\gamma$, if the step size $\Delta\gamma$ is too large. The orbit of p would then diverge to infinity.

3.3. **The annually forced system: quasi-periodicity and chaos.** In this section we study the AMO mode under periodic forcing modelling annual variations in the surface heat flux. In this setting we detect a Hopf-Neĭmark-Sacker bifurcation which gives rise to an invariant 2-torus. The dynamics on this torus correspond to the periodic forcing imposed on the AMO mode.

Forcing heat flux. Define

$$Q_{\text{per}} = (1-\gamma)Q_{\text{rest}} + \gamma Q_{\text{pres}} + P(t)S(x,y)$$

Here, P and S are functions setting the time scale and spatial structure of the forcing, respectively. We set

$$P(t) = \epsilon \cos\left(\frac{2\pi t}{\mathcal{T}}\right)$$

and

$$S(x,y) = \frac{1}{4}\left[1 - \cos\left(\frac{2\pi x}{L_x}\right)\right]\left[1 - \cos\left(\frac{2\pi y}{L_y}\right)\right],$$

where the parameters ϵ and $\mathcal{T}$ denote the strength and the period of the forcing, respectively. We will set $\mathcal{T} = 365$ days (unless specified otherwise), and for ϵ we will use values in the range of 0.1 to 1.0. The value $\epsilon = 0.5$ corresponds approximately to 10% of the difference between the maximum and minimum over the basin of the heat flux Q_{pres}. The periodic component $P(t)S(x,y)$ can be interpreted as a very rough approximation to fluctuations observed in surface heat fluxes over the North Atlantic (Cayan [11]).

Amplification of the AMO mode. We now fix the equator-to-pole temperature gradient at $\Delta T = 20$ and the forcing period $\mathcal{T} = 365$ days. For $\gamma = 0.95$ the autonomous system ($\epsilon = 0$) has an equilibrium destabilising through a supercritical Hopf bifurcation which gives rise to the AMO mode. In the periodically forced system ($\epsilon > 0$) a stable periodic orbit bifurcates into an attracting 2-dimensional torus through a Hopf-Neĭmark-Sacker bifurcation where two complex conjugate Floquet multipliers cross the unit circle. This bifurcation takes place for almost the same value of γ for which the corresponding Hopf bifurcation occurred in the autonomous system $\epsilon = 0$.

In physical terms, the dynamics on the 2-torus attractor corresponds to the annual cycle imposed on the original AMO signal, see Figure 13. For most parameter values the dynamics on the 2-torus is quasi-periodic. Only for parameter values in very narrow domains the periods of the forcing and of the AMO mode become commensurate, which leads to a periodic attractor on the 2-torus. The size of the forcing amplitude ϵ determines the size of the 2-torus (in state space), or equivalently, the amplification of the AMO.

Figure 13 shows the peak-to-peak amplitude of the basin averaged sea surface temperature as function of the forcing period $\mathcal{T}$ for different values of ϵ. For fixed $\mathcal{T}$ the variability increases with increasing ϵ. For fixed ϵ a larger value of $\mathcal{T}$ (i.e., a lower forcing frequency) is more effective in amplifying the AMO mode. Observe that for the different values of ϵ the variability is linear in $\mathcal{T}$. In addition, the slopes are linear functions of ϵ: computing a linear fit gives

$$\text{peak-to-peak SST} = a + (c + d\epsilon)\mathcal{T},$$

where $a = 0.938549$, $c = -0.00135510$, and $d = 0.00116036$.

The Poincaré map and its attractors. The state space of the periodically forced system is 28-dimensional and is given by the Cartesian product of a circle (containing the time-periodicity) with the 27-dimensional state space of the autonomous system. A convenient way to study this system is by means of a Poincaré map (also referred to as a time-$\mathcal{T}$ map or stroboscopic map). This map is obtained numerically by sampling the integration output of the periodically forced system at integer multiples of the forcing period $\mathcal{T}$. This procedure reduces the dimension of the state space by one and gives a discrete time dynamical system with a 27-dimensional state space. Moreover, the complexity of attractors is reduced: a invariant 2-torus becomes an invariant circle, and a periodic orbit becomes a periodic point. In what follows, the Poincaré map will be denoted by P.

Now we fix the parameters $\epsilon = 0.25$ and $\mathcal{T} = 365$ and give an overview of the attractors that occur for various values in the $(\Delta T, \gamma)$-plane. An overview of the dynamics of the Poincaré map P is obtained by brute force iteration. We fix the value of ΔT and increase the value of γ from 0.995 up to 1.0 in steps of 10^{-5}. For each value of γ we compute 10^4 iterates of P and plot the last 500 computed points; the final point of the last attractor serves as an initial condition for the next loop. Simultaneously we compute the three largest Lyapunov exponents to classify the attractor. See Figure 14 and Figure 15. Note that by this procedure we cannot detect multistability, i.e., the coexistence of different attractors. This can be detected by using more refined procedures with varying initial conditions. Also observe that the second Lyapunov exponent is always negative but increases to zero when the amount of damping (controlled by γ) is decreased.

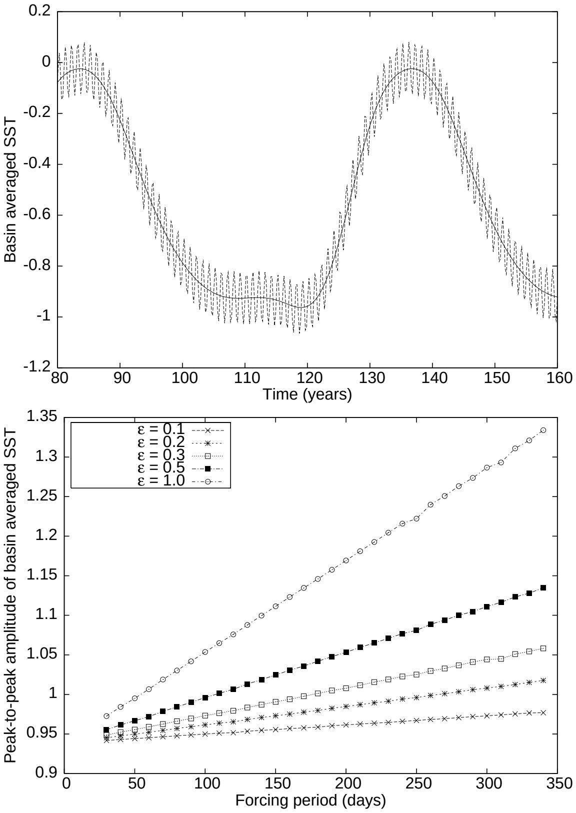

FIGURE 13. Top panel: time series of the AMO mode (solid) and a quasi-periodic attractor obtained with periodic forcing for $\epsilon = 0.5$ and $\mathcal{T} = 365$ days (dashed). The basin averaged sea surface temperature is plotted against the time in years. Bottom panel: The peak-to-peak amplitude of the basin averaged sea surface temperature as a function of the forcing period (in days) for different values of ϵ.

As in the autonomous case, we also found attractors for values $\gamma > 1$. However, orbits may escape to infinity depending on the initial point, see a remark at the end of Section 3.2.

Quasi-periodic and periodic dynamics. For most values of the parameters the dynamics of P is quasi-periodic, meaning that evolutions densely fill an invariant circle. Only in narrow windows of the $(\Delta T, \gamma)$-parameter plane phase locking can be observed, where the dynamics on the invariant circle locks onto a periodic point attractor, as in Figure 16. This behaviour occurs when parameter values move through so-called Arnol′d tongues. These are regions in the $(\Delta T, \gamma)$-plane bounded by pairs of curves of saddle-node bifurcations of periodic orbits originating from a common resonant Hopf-Neĭmark-Sacker bifurcation. It is precisely in these regions where the periods of the forcing and the AMO mode become commensurate.

Quasi-periodic period doublings. The periodically forced system exhibits quasi-periodic period doublings of the P-invariant circle. These bifurcations can be seen

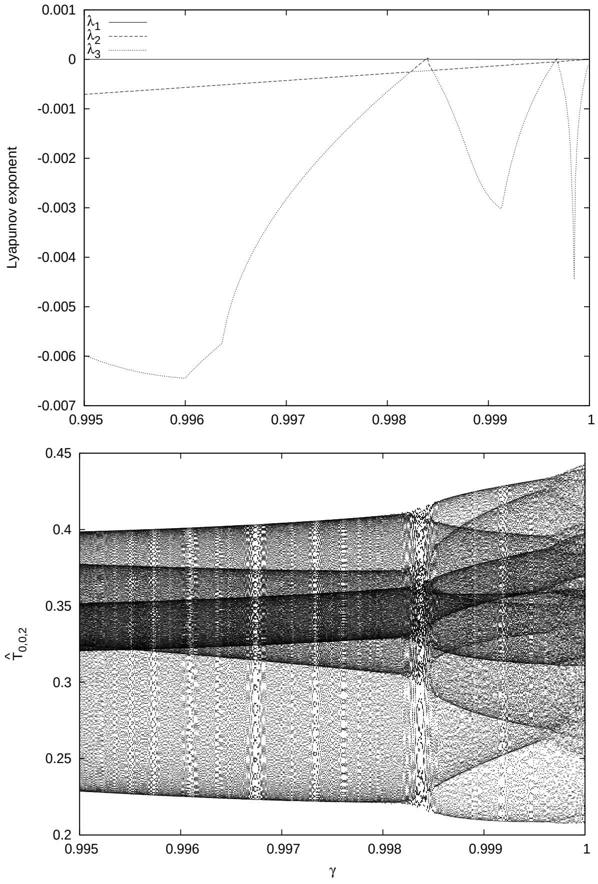

FIGURE 14. Top: the three largest Lyapunov exponents $\lambda_{1,2,3}$ as a function of γ for $\Delta T = 22$. Bottom: projections on $\widehat{T}_{0,0,2}$ of attractors of the Poincaré map as a function of γ.

as perturbations arising for $\epsilon > 0$ from the period doublings in the autonomous system, see Section 3.2 and Figure 10. Indeed, the values of γ where the quasi-periodic period doublings occur for $\epsilon > 0$ are close to those where period doublings occur for $\epsilon = 0$. Period doubling bifurcations can be identified in the Lyapunov diagrams of Figure 14 and Figure 15 as the locations where the second Lyapunov exponent becomes zero.

Only two period doublings are detected up to $\gamma = 1$ for $\Delta T = 22$°C. At least eleven doublings are detected for $\Delta T = 24$°C, but only three of them can be seen in the Lyapunov diagram due to the large step size in γ. The parameter values of the first eleven doublings are listed in Table 2, and we expect that they are followed by infinitely many additional period doublings. Figure 17 shows a sequence of doubled invariant circles which are born at the first four period doublings.

Note, however, that further refinement of the values in Table 2 requires a huge computational effort. For a careful determination of the location of the period doubling the Lyapunov exponents have to be determined with an error below 10^{-6}.

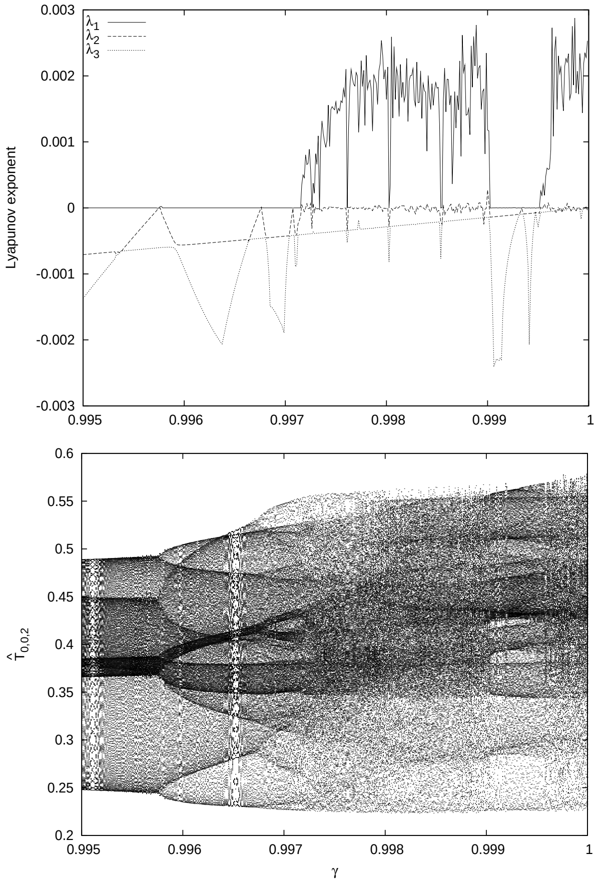

FIGURE 15. Top: the three largest Lyapunov exponents $\lambda_{1,2,3}$ as a function of γ for $\Delta T = 24$. Bottom: projections on $\widehat{T}_{0,0,2}$ of attractors of the Poincaré map as a function of γ.

This requires a great number of Poincaré iterates, and usage of extrapolation techniques, see, e.g., Broer and Simó [4] and Simó [37]. Up to 5×10^6 iterates have been used for some selected values of γ after a transient of 10^6 iterates. See Section B.2 for additional details and illustrations.

Two different types of quasi-periodic period doubling bifurcations are possible (see Broer *et al.* [2]): as a parameter is varied, an attracting invariant circle loses stability and gives birth

1. to a single attracting invariant circle of roughly double length;
2. to a pair of disjoint circles, each mapped onto the other by the Poincaré map P. This is also referred to as a pair of periodically invariant circles of period 2, or a period-2 invariant circle.

A priori there is no reason to expect that only one of the two types occurs, but in our model we only have found period doublings of length-doubling type. In cases where the invariant torus is reducible, the type of bifurcation can be deduced from the eigenvalues of an associated Floquet matrix, see Jorba [29] and Broer *et al.* [7, 45] for details.

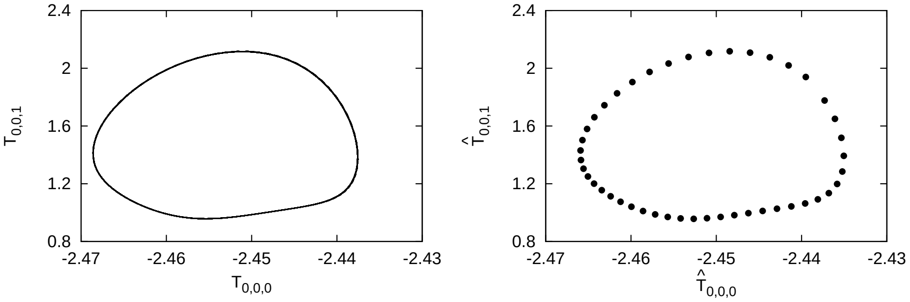

FIGURE 16. Two different attractors of the Poincaré map for $\Delta T = 22$. Left panel: an invariant circle with quasi-periodic dynamics ($\gamma = 0.9967347$). Right panel: a periodic point attractor ($\gamma = 0.9967379$) having period 45.

Remark 1. A full description of the quasi-periodic period doubling bifurcation of invariant circles requires in fact two parameters. Loosely speaking, one parameter is necessary to unfold the loss of normal hyperbolicity and another parameter is required to enforce a Diophantine condition for the rotation number, necessary for KAM-like persistence of the 'undoubled' invariant circle, see Broer *et al.* [1, 5, 9, 7, 8].

In 2-dimensional parameter space the quasi-periodic bifurcation set is a Cantor set which is contained in a smooth curve, its gaps being filled with resonance bubbles, giving rise to a 'frayed' boundary. The quasi-periodic doubling bifurcation admits a simple description only if parameters are restricted to any of the codimension one manifolds (curves in parameter space) where the rotation number is Diophantine. Much more intricate bifurcation structures are expected within the resonance 'bubbles', but the quasi-periodic bifurcation theory does not predict the generic behaviour there, see Broer *et al.* [7] for a case-study of the quasi-periodic Hopf bifurcation.

When varying only one parameter from panel (A) to (B) in Figure 17, the theory predicts that a quasi-periodic doubling occurs with positive probability, although one cannot exclude that a resonance 'bubble' is being crossed instead. See Broer *et al.* [7, 45] and Chenciner [13, 14, 15] for a more complete discussion.

From the parameter values in Table 2 (see also Figure 19 in Appendix B.2) we conjecture that

$$\lim_{n\to\infty} q_n = F,$$

where $F \approx 4.6692$ is Feigenbaum's constant. The end of the period doubling cascade, γ_∞, will be located very close to $\gamma = 0.997150334$. Observe in Figure 15 that, despite the spacing in γ is too large, this is indeed the approximate location for which the dominant Lyapunov exponent becomes positive. In similar models it is common that only a *finite number* of period doublings appears, see e.g. Broer *et al.* [45], but in the present model and for $\Delta T = 24$ it seems that the full cascade is present.

Strange attractors. For $\gamma = 0.997185$, the strange attractor in Figure 18 (left panel) is detected. On this type of attractors the dynamics is chaotic: the dominant

n	γ_n	$q_n = \frac{\gamma_n - \gamma_{n-1}}{\gamma_{n+1} - \gamma_n}$	n	γ_n	$q_n = \frac{\gamma_n - \gamma_{n-1}}{\gamma_{n+1} - \gamma_n}$
1	0.9957520		7	0.997150177	4.7
2	0.99675927	3.18	8	0.997150300	4.6
3	0.99707620	5.46	9	0.9971503270	4.8
4	0.997134254	4.59	10	0.99715033265	4.8
5	0.997146898	4.68	11	0.99715033382	
6	0.997149598	4.66			

Table 2. Approximate locations of the first eleven quasi-periodic period doublings for $\Delta T = 24$. In the third column the ratios of the successive distances between the bifurcations are listed.

γ	Figure	λ_1	λ_2	λ_3
0.99650	Figure 17A	$+3.2 \times 10^{-7}$	-4.9×10^{-4}	-1.2×10^{-3}
0.99700	Figure 17B	-2.2×10^{-7}	-4.2×10^{-4}	-1.3×10^{-3}
0.99709	Figure 17C	-6.0×10^{-7}	-4.1×10^{-4}	-8.9×10^{-4}
0.99714	Figure 17D	-1.8×10^{-7}	-1.9×10^{-4}	-4.0×10^{-4}
0.997185	Figure 18	$+4.5 \times 10^{-4}$	-5.8×10^{-5}	-4.0×10^{-4}

Table 3. Lyapunov exponents for the attractors shown in the listed Figures.

γ	Number of windings	γ	Number of windings
0.997261	10-circle	0.998026	7-circle
0.997450	11-circle	0.998536	11-circle
0.997540	6-circle	0.998554	doubled 11-circle
0.997546	doubled 6-circle	0.999025	4-circle
0.997606	5-circle	0.999355	doubled 4-circle
0.997615	doubled 5-circle	0.999499	quadrupled 4-circle

Table 4. Values of γ in the chaotic range for $\Delta T = 24$ for which invariant circles occur and their number of windings.

Lyapunov exponent is positive, which means that nearby evolutions separate in an exponentially fast way.

The structure of the attractor is visualised by a 'slice', that is points contained in thin layers (width 5.0×10^{-3}) centred around hyperplanes of the form $\{\widehat{T}_{0,0,1} = 1.8\}$, see Figure 18 (right panel). Observe that points in this slice are rather scattered. We emphasize that this is not an error in the computations. Nor it is due to the chosen thickness of the slice: the 'fuzzyness' of points in the slice persists when the thickness of the slice is reduced. The reason for the fuzzyness can be explained by wild foldings of an unstable manifold as in the case of the Hénon-like attractor of Figure 12.

The attractor shown in Figure 18 is reminiscent of the so-called quasi-periodic Hénon-like strange attractors, which are formed by the closure of the unstable manifold of an invariant circle of saddle-type (Broer *et al.* [6]). These attractors have been detected numerically in a seasonally forced Lorenz-84 model studied by

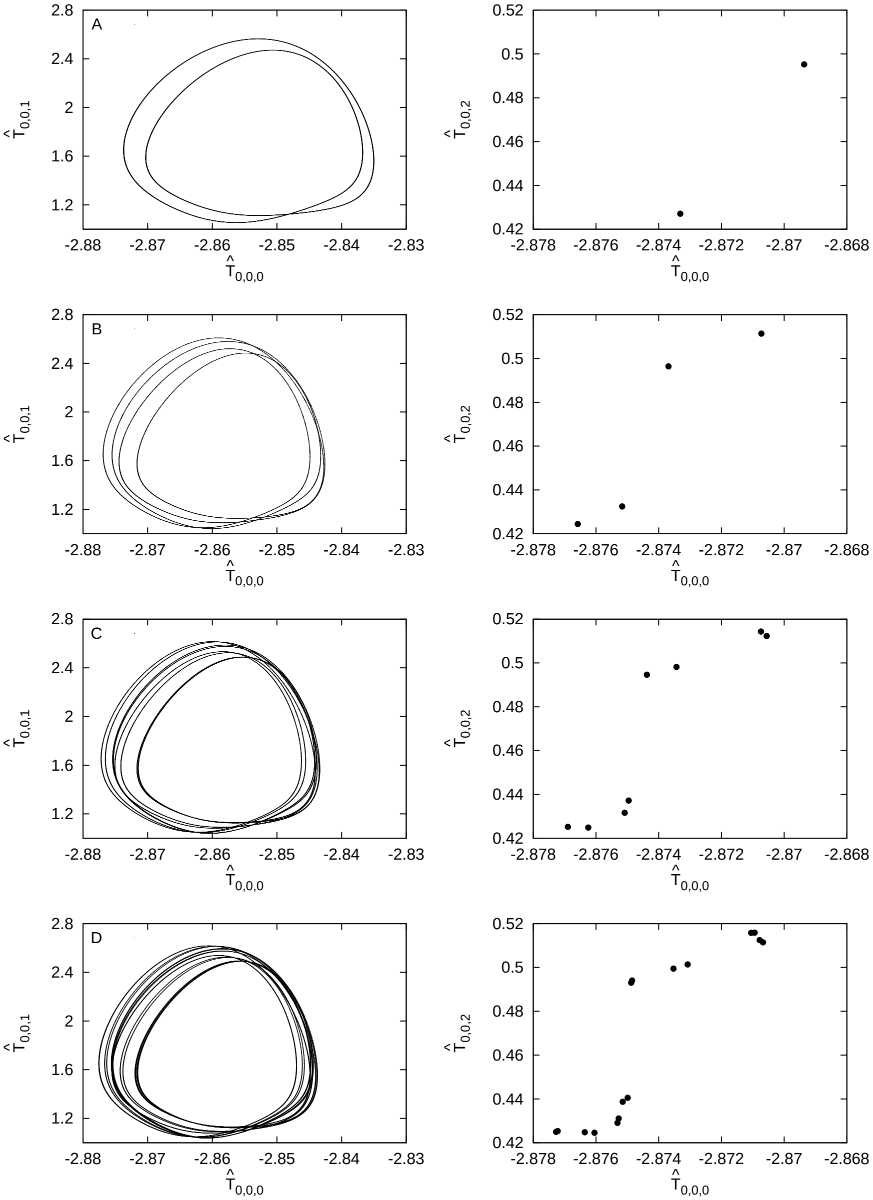

FIGURE 17. Invariant circles of the Poincaré map for $\Delta T = 24$ appearing after the first four period doublings. See Table 3 for the values of γ and Lyapunov exponents. Left panels: projections on $(\widehat{T}_{0,0,0}, \widehat{T}_{0,0,1})$. Right panels: projections on $(\widehat{T}_{0,0,0}, \widehat{T}_{0,0,2})$ of the points belonging to the fattened slice $|\widehat{T}_{0,0,1} - 1.8| \leq 5.0 \times 10^{-3}$.

Broer *et al.* [5]. In that case, both types of quasi-periodic doublings (1 and 2 above) have been found to occur in the same sequence, and the strange attractor appears when a homoclinic tangency of a saddle-periodic point destroys the twice-doubled invariant circle.

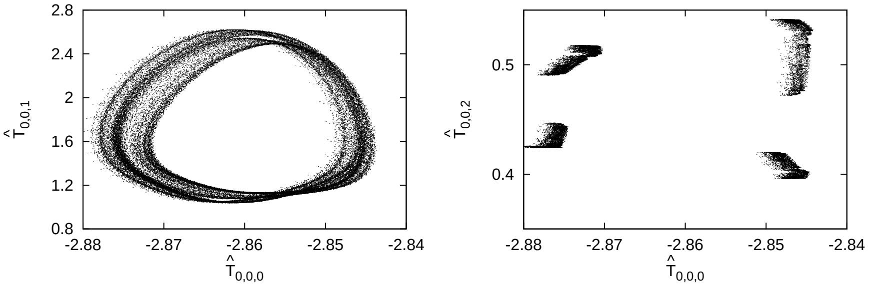

FIGURE 18. Strange attractor of the Poincaré map for $\Delta T = 24$ appearing after the end of the period doubling cascade. Top panel: projection on $(\widehat{T}_{0,0,0}, \widehat{T}_{0,0,1})$. Bottom panel: projections on $(\widehat{T}_{0,0,0}, \widehat{T}_{0,0,2})$ of the points belonging to the fattened slice $|\widehat{T}_{0,0,1} - 1.8| \leq 5.0 \times 10^{-3}$.

Invariant circles in the chaotic range. From Figure 15 it is evident that the range of values of γ for which the dominant Lyapunov exponent is positive is interrupted with small windows for which the dominant Lyapunov exponent is zero. This means that the parameter domains characterised by the occurrence of strange attractors are interrupted by parameter sets where invariant circles occur. In turn, these invariant circles can bifurcate again through quasi-periodic period doublings. This scenario is similar to what happens in cascades of period doublings for periodic orbits, cf. Figure 10.

The invariant circles can be detected numerically by taking small step sizes ($\Delta\gamma < 3 \times 10^{-6}$) in the chaotic range and brute force iteration of the Poincaré map. This procedures results shows the existence of invariant circles with a number of windings that differs from window to window. A summary of the results is presented in Table 4.

4. Summary and discussion.

In this paper we have studied the dynamics of a model for the Atlantic Multidecadal Oscillation. Instead of using the traditional high-dimensional models (often obtained by finite-difference discretisation schemes) we have derived a low-order model by means of a Galerkin projection of the governing equations onto a finite-dimensional function space.

Results. The AMO appears in our model due to a supercritical Hopf bifurcation of a stable equilibrium (associated with a steady ocean flow) by switching from restoring to prescribed heat flux (i.e., by increasing the parameter γ from 0 to 1). This is the typical bifurcation scenario associated with the AMO, see Te Raa and Dijkstra [40] and Dijkstra *et al.* [21]. In addition, our low-order model captures the physical signatures of the AMO: the multidecadal period, the westward propagation of sea surface temperature anomalies, and the phase difference between the meridional and zonal overturning anomalies. The period doubling bifurcations of the periodic orbit associated with the AMO have also been detected in high-dimensional models studied in Te Raa *et al.* [42].

The new element of this study is the introduction of periodic forcing in the surface heat flux which can be interpreted as an annual cycle. Then, the stable equilibria of the low-order model are replaced by stable periodic orbits. In particular, the

AMO now appears as a quasi-periodic attractor through a Hopf-Neĭmark-Sacker bifurcation of the periodic attractor associated with the annual cycle. For most parameter values the dynamics is quasi-periodic which means that the periods of the AMO and the annual cycle are incommensurate. In turn, the 2-torus can undergo various quasi-periodic period doublings, and this leads to strange attractors which are reminiscent to the quasi-periodic Hénon-like strange attractors discussed in Broer *et al.* [5, 6].

The results of this paper provide ample motivation for further investigations of both mathematical and physical topics.

Mathematical issues. Our low-order model is derived from a dynamical system with an infinite-dimensional state space viz. a system of five partial differential equations. It is a natural question whether the numerically observed dynamics in our low-order model has any relation with the original infinite-dimensional system and what part of the dynamics persists as the number of retained basis functions in the Galerkin projection is increased. For this it is at least necessary to have a better understanding of the state space of the original infinite-dimensional system, e.g., by proving the existence of weak solutions and global attractors or inertial manifolds along the lines of Robinson [36] or Temam [43].

Physical issues. The dynamically interesting results are obtained near the parameter value $\gamma = 1$, i.e., for forcing conditions which are almost prescribed. However, prescribed heat flux in ocean models is a strong idealisation since it amounts to net zero atmospheric damping—in reality sea surface temperature anomalies are substantially damped by the atmosphere. It is expected that 'realistic' values of γ satisfy $\gamma < \gamma_{\mathrm{H}}$ which implies that the AMO mode is damped (see Dijkstra *et al.* [21]). On the other hand, it is known that the atmosphere itself exhibits variability on various time and spatial scales. This leads to the following question:

> Can atmospheric variability excite the weakly damped AMO mode?

Here, excitation means that multidecadal variability related to the AMO can be observed for parameter values $\gamma < \gamma_{\mathrm{H}}$.

This question has been addressed by Dijkstra *et al.* [21] and Frankcombe *et al.* [24] by studying an ocean-only model where stochastic noise is used to model atmospheric variability. It was found that stochastic noise indeed excites the AMO mode which is interpreted as a stochastic Hopf bifurcation. Moreover, white noise only weakly excites the AMO mode, but the introduction of spatial and temporal coherence in the forcing can increase the amplitude of the variability to levels corresponding with observations.

Current research by the authors is investigating whether intermittent atmospheric behaviour may be involved in the excitation of the AMO. We adopt again the setting of deterministic low-order models, where detailed dynamical analysis can be carried out. As a starting point, the model described in this paper is being coupled to the low-order atmospheric model of Sterk *et al.* [39].

Acknowledgements. AES is supported by the Netherlands Organisation for Scientific Research (NWO) by grant ALW 854.00.036. RV gratefully acknowledges support of the Willis Research Network (www.willisresearchnetwork.com). The research of CS has been supported by grant MTM2006-05849/Consolider (Spain). The University of Barcelona is kindly thanked for its hospitality. The authors gratefully acknowledge financial support from the University of Groningen for a mini symposium on dynamical systems held on September 17 and 18, 2009.

The authors thank Leela Frankcombe (IMAU/UU) for making Figure 1. The (anonymous) reviewer is kindly thanked for useful comments which helped to improve the presentation of this paper.

Appendix A. Coefficients of the low-order model. In the Galerkin projection the fields T, ψ, and ϕ are replaced by the truncated series expansions. The resulting equations are multiplied with the basis functions and integrated over the spatial domain. This gives a set of ordinary differential equations for the time-dependent expansion coefficients.

The coefficients in the equations for the low-order model are given by integrals of (products of) the basis functions, which are readily implemented in an algebraic manipulation program. To simplify the notation of the formulas below we will omit subscripts of the summations signs—indices of the vectors $\widehat{T}$ run through the set R_T, and indices of the vectors $\widehat{\psi}$ and $\widehat{\phi}$ run through the set R_S (see Section 2.2).

The thermal wind balance. The equations (2)-(4) are so-called *diagnostic equations*, i.e., they do not contain derivatives with respect to time. The Galerkin projections of these equations are linear algebraic equations from which we can compute the expansion coefficients for the velocity potentials in terms of the expansion coefficients of the temperature field.

After substitution of the stream functions, the thermal wind balance is given by

$$-E_H\left(\frac{\partial^3\psi}{\partial x^2\partial z}+\frac{\partial^3\psi}{\partial y^2\partial z}\right)-E_V\frac{\partial^3\psi}{\partial z^3}+\frac{\partial\phi}{\partial z} = \frac{\partial p}{\partial x}, \tag{13}$$

$$E_H\left(\frac{\partial^3\phi}{\partial x^2\partial z}+\frac{\partial^3\phi}{\partial y^2\partial z}\right)+E_V\frac{\partial^3\phi}{\partial z^3}+\frac{\partial\psi}{\partial z} = \frac{\partial p}{\partial y}, \tag{14}$$

$$Ra\,T = \frac{\partial p}{\partial z}. \tag{15}$$

After the Galerkin projection we obtain the following system of linear equations:

$$\begin{aligned}\sum M_{(p,q,r),(m,n,k)}\widehat{\psi}_{p,q,r}-C_{(p,q,r),(m,n,k)}\widehat{\phi}_{p,q,r} &= f_{(m,n,k)},\\ \sum M_{(p,q,r),(m,n,k)}\widehat{\phi}_{p,q,r}+C_{(p,q,r),(m,n,k)}\widehat{\psi}_{p,q,r} &= g_{(m,n,k)}.\end{aligned}$$

In these equations, the coefficients due to mixing of momentum are given by

$$\begin{aligned}M_{(p,q,r),(m,n,k)} = {}& E_H\int_0^1 b_p''(x)b_m(x)dx\int_0^1 b_q(y)b_n(y)dy\int_{-1}^0 s_r'(z)s_k'(z)dz\\ &+E_H\int_0^1 b_p(x)b_m(x)dx\int_0^1 b_q''(y)b_n(y)dy\int_{-1}^0 s_r'(z)s_k'(z)dz\\ &+E_V\int_0^1 b_p(x)b_m(x)dx\int_0^1 b_q(y)b_n(y)dy\int_{-1}^0 s_r'''(z)s_k'(z)dz\end{aligned}$$

and the coefficients due to the Coriolis force are given by

$$C_{(p,q,r,),(m,n,k)} = \int_0^1 b_p(x)b_m(x)dx\int_0^1 b_q(y)b_n(y)dy\int_{-1}^0 s_r'(z)s_k'(z)dz.$$

Finally, the coefficients of the right hand side are given by

$$\begin{aligned} f_{(m,n,k)} &= -Ra \sum \widehat{T}_{p,q,r} \int_0^1 c_p(x) b'_m(x) dx \int_0^1 c_q(y) b_n(y) dy \int_{-1}^0 c_r(z) s_k(z) dz, \\ g_{(m,n,k)} &= Ra \sum \widehat{T}_{p,q,r} \int_0^1 c_p(x) b_m(x) dx \int_0^1 c_q(y) b'_n(y) dy \int_{-1}^0 c_r(z) s_k(z) dz. \end{aligned}$$

Observe that we have eliminated the pressure gradient from the projected equations. Indeed, by performing an integration by parts the pressure gradient vanishes since a gradient is orthogonal to a divergence-free field with a vanishing normal component at the boundary.

The advection equation. The equation (6) is a so-called *prognostic* equation, i.e., containing a derivative with respect to time. The Galerkin projection of this equation is a system of ordinary differential equations with quadratic nonlinearities for the time-dependent expansion coefficients of the temperature field.

After substitution of the stream functions, the advection equation is given by

$$\begin{aligned} \frac{\partial T}{\partial t} - \frac{\partial \psi}{\partial z}\frac{\partial T}{\partial x} + \frac{\partial \phi}{\partial z}\frac{\partial T}{\partial y} + \left(\frac{\partial \psi}{\partial x} - \frac{\partial \phi}{\partial y}\right)\frac{\partial T}{\partial z} = P_H \left(\frac{\partial^2 T}{\partial x^2} + \frac{\partial^2 T}{\partial y^2}\right) + P_V \frac{\partial^2 T}{\partial z^2} \\ + B(T_S - (T + T_0))g(z). \end{aligned}$$

The projected equation is given by

$$\begin{aligned} \frac{d\widehat{T}_{m,n,k}}{dt} = \sum \alpha_{(p,q,r),(h,i,j),(m,n,k)} \widehat{\psi}_{p,q,r} \widehat{T}_{h,i,j} + \beta_{(p,q,r),(h,i,j),(m,n,k)} \widehat{\phi}_{p,q,r} \widehat{T}_{h,i,j} \\ + D_{(m,n,k)} \widehat{T}_{m,n,k} + \sum \gamma_{(p,q,r),(m,n,k)} (\widehat{T}_{S,p,q,r} - \widehat{T}_{p,q,r}). \end{aligned}$$

In this equation, the coefficient $\alpha_{(p,q,r),(h,i,j),(m,n,k)}$ equals

$$\begin{aligned} \int_0^1 b'_p(x) c_h(x) c_m(x) dx \int_0^1 b_q(y) c_i(y) c_n(y) dy \int_{-1}^0 s_r(z) c'_j(z) c_k(z) dz \\ - \int_0^1 b_p(x) c'_h(x) c_m(x) dx \int_0^1 b_q(y) c_i(y) c_n(y) dy \int_{-1}^0 s'_r(z) c'_j(z) c_k(z) dz \end{aligned}$$

and the coefficient $\beta_{(p,q,r),(h,i,j),(m,n,k)}$ equals

$$\begin{aligned} \int_0^1 b_p(x) c_h(x) c_m(x) dx \int_0^1 b_q(y) c'_i(y) c_n(y) dy \int_{-1}^0 s'_r(z) c_j(z) c_k(z) dz \\ - \int_0^1 b_p(x) c_h(x) c_m(x) dx \int_0^1 b'_q(y) c_i(y) c_n(y) dy \int_{-1}^0 s_r(z) c'_j(z) c_k(z) dz \end{aligned}$$

The dissipation coefficients are given by

$$D_{(m,n,k)} = -\pi^2 \left[P_H(m^2 + n^2) + P_V k^2\right]$$

Finally, the coefficients of the forcing terms are given by.

$$\gamma_{(p,q,r)} = \int_0^1 c_p(x) c_m(x) dx \int_0^1 c_q(y) c_n(y) dy \int_{-1}^0 c_r(z) c_k(z) g(z) dz.$$

Appendix B. **Numerical analysis of the low-order model.** The low-order model is numerically investigated using continuation and integration techniques. For continuation we have used the program AUTO–07p (Doedel and Oldeman [22]), and most of the technology behind this software is described in Kuznetsov [33].

For numerical integration and the computation of Lyapunov exponents we have written our own software, and we briefly describe the algorithms below.

B.1. **The Taylor integrator.** The low-order model can be written symbolically as

$$\frac{dx_i}{dt} = C_i + \sum_{j=1}^{d} L_{ij}x_j + \sum_{j,k=1}^{d} Q_{ijk}x_jx_k, \quad i = 1, \dots, d, \tag{16}$$

where $d = 27$ is the dimension of the state space. This system is integrated numerically by computing a truncated Taylor expansion of the solution around time t_0:

$$x_i(t_0 + h) = \sum_{n=0}^{N} x_i^{[n]}(t_0)h^n + O(h^{N+1}),$$

where the coefficients are given by

$$x_i^{[n]}(t_0) := \frac{1}{n!}\left.\frac{d^nx_i}{dt^n}\right|_{t=t_0}. \tag{17}$$

Given a point $x_i^{[0]}(t_0)$, which is either an initial condition or a previously computed point on the trajectory, we first compute

$$x_i^{[1]} = C_i + \sum_{j=1}^{d} L_{ij}x_j^{[0]} + \sum_{j,k=1}^{d} Q_{ijk}x_j^{[0]}x_k^{[0]}.$$

Then, for $n > 0$, we have the recurrent relation

$$x_i^{[n+1]} = \frac{1}{n+1}\left(\sum_{j=1}^{d} L_{ij}x_j^{[n]} + \sum_{j,k=1}^{d}\sum_{m=0}^{n} Q_{ijk}x_j^{[m]}x_k^{[n-m]}\right),$$

which follows by substituting the truncated Taylor series in (16) using the Leibniz rule for differentiation of products.

We have chosen a tolerance $\epsilon = 10^{-16}$. This gives $N = 20$ as the optimal order. The step size is then computed as $h_m = \min\{s_{m,1}, s_{m,2}\}$, where

$$s_{m,1} = \exp\left\{\frac{1}{N-1}\log\left(\epsilon\frac{\|x^{[1]}\|_\infty}{\|x^{[N]}\|_\infty}\right)\right\},$$
$$s_{m,2} = \exp\left\{\frac{1}{N-2}\log\left(e^2\epsilon\frac{\|x^{[1]}\|_\infty}{\|x^{[N-1]}\|_\infty}\right)\right\}.$$

A very convenient aspect of the Taylor integration method is the possibility of producing dense output by just evaluating the Taylor polynomial at time $t + h$ for any desired value of $h < h_m$; the cost of evaluating the Taylor polynomial is negligible in comparison to the computation of the coefficients.

The reader is referred to Jorba and Zou [30] for a detailed discussion on the Taylor method and a ready-to-use implementation.

B.2. **Computing Lyapunov exponents and detecting the period doubling cascade.** Lyapunov exponents are computed as described in Simó [37]. After a transient of L iterates of the Poincaré map P, let $x^{(0)}$ be the current point on the orbit. In order to compute k Lyapunov exponents, we randomly generate a set of orthonormal vectors ξ_j $(j = 1, \dots, k)$. The differential of the Poincaré map is applied to the ξ_j obtaining the vectors $\eta_j = DP(x^{(0)})\xi_j$. The vectors η_j are orthogonalised (not yet normalised) to obtain vectors ζ_j. The vectors ζ_j are normalised to obtain the new vectors ξ_j and a new point is computed on the orbit: $x^{(1)} = P(x^{(0)})$. The process is iterated up to a maximum of N iterates. From this procedure we compute the so-called *Lyapunov sums*

$$S_j(n) = \sum_{i=1}^{n} \log \|\zeta_j(n)\|_2$$

as a function of the number of iterations n.

The Lyapunov exponents are computed as the limit slopes of the sequences $S_j(n)$ as follows. Every M iterates of the Poincaré map we compute a linear fit for the points $(n, S_j(n))$ based on the last fraction α_i $(i = 1, 2, 3)$ of the iterations; this gives the slopes $s_j^{(i)}$. We stop the computations if either the maximum number of

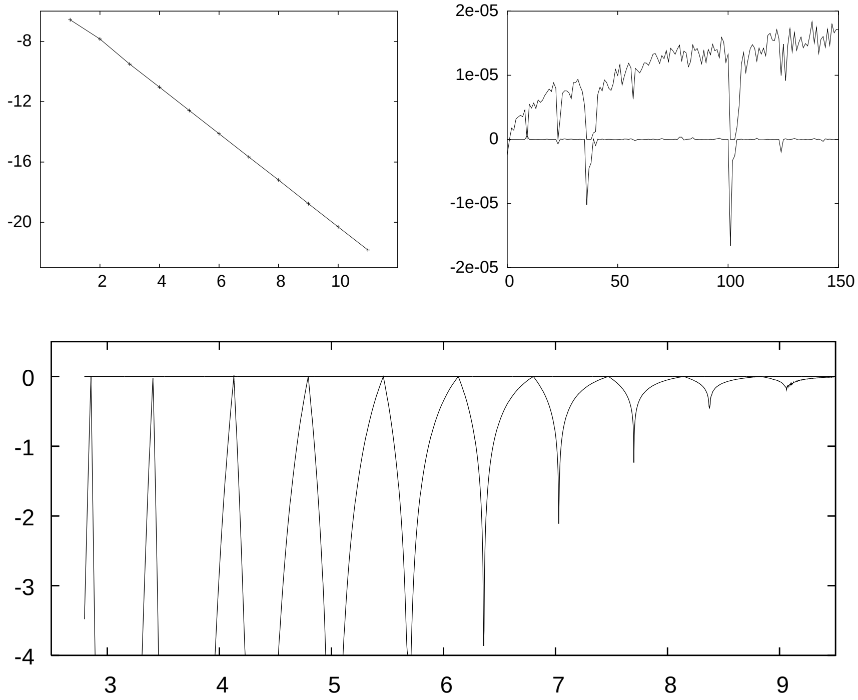

FIGURE 19. Top left: $\log(\ell - \gamma_n)$ is plotted as a function of n, where $\ell \approx 0.99715033413$ is the estimated limit of the cascade. Top right: Lyapunov exponents after the end of the cascade as a function of γ. The horizontal variable is $10^{10} \times (\gamma - 0.997150334)$. Bottom: The cascade is visualised by plotting the first two Lyapunov exponents, multiplied by 10^4, as a function of $-\log_{10}(\ell - \gamma)$.

iterations N is exceeded or when the slopes satisfy

$$\Delta := \max_{j=1,\dots,k} \{|s_j^{(1)} - s_j^{(2)}|, |s_j^{(3)} - s_j^{(2)}|\} < \mu,$$

where μ is a given tolerance. The last computed $s_j^{(2)}$ are used as estimates for the Lyapunov exponents and the last value of Δ is used as an estimate for the error. Typical values used in the computations are

$$k = 3,\ L = 10^5,\ M = 10^4,\ N = 10^6,\ \alpha_1 = 0.2,\ \alpha_2 = 0.4,\ \alpha_3 = 0.6.$$

The computation is especially delicate if Lyapunov exponents are used to detect period doubling of invariant curves, because then the error should be small. The values in Table 2 are obtained with the values of parameters given above and typical errors in the Lyapunov exponents are $\approx 10^{-6}$. This is checked by repeating computations with different random seeds. Figure 19 shows the estimated behaviour of the accumulation of γ_n to a limit value, the evidence of the existence of strange attractors shortly after the limit and the different bifurcations in a suitable scale.

Finally, we consider it also relevant to display the behaviour of the Lyapunov sums as a function of the number of iterates. In the reducible case (Jorba [29] and Broer *et al.* [4, 45]) we can expect the typical pattern of a linear system modulated by a quasi-periodic change of variables. This is what can be guessed from Figure 20 left, which corresponds to $\gamma \approx \gamma_4$. Similar patterns are seen for smaller values of γ. For larger γ, as in Figure 20 right for $\gamma \approx \gamma_{10}$, slightly wilder patterns are detected. They become much more wild beyond the end of the cascade, see Figure 20 bottom.

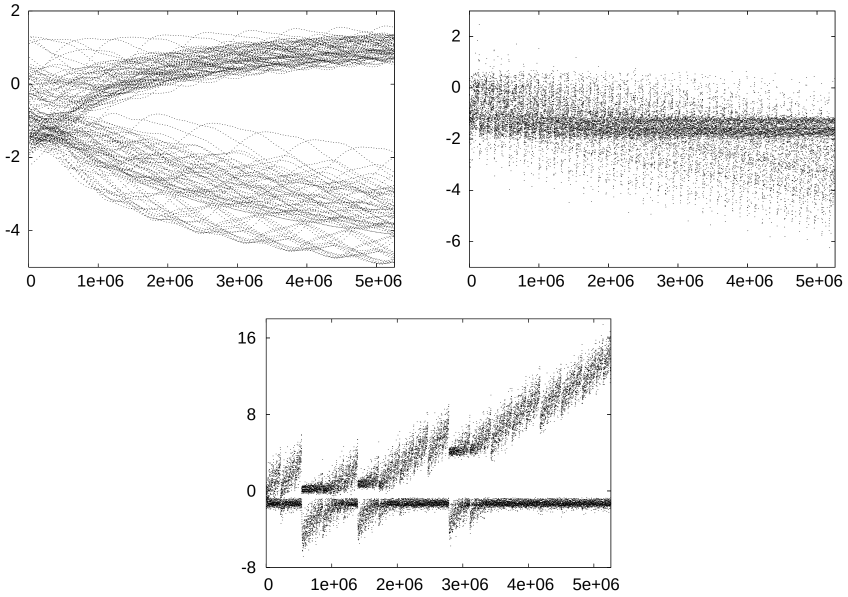

FIGURE 20. First two Lyapunov sums as a function of time. A transient with $L = 10^6$ followed by $M = 10^6$ additional iterates of the Poincaré map has been used. Only one point every 100 iterates is plotted. Top left: The value of γ is close to γ_4. Top right: The value of γ is close to γ_{10}. Bottom: $\gamma = 0.997150335$, after the end of the period doubling cascade.

REFERENCES

[1] H.W. Broer, G.B. Huitema and M.B. Sevryuk, "Quasi-periodic Motions in Families of Dynamical Systems, Order amidst Chaos," Lecture Notes in Mathematics **1645**, Springer-Verlag, Berlin, 1996.

[2] H.W. Broer, G.B. Huitema, F. Takens and B.L.J. Braaksma, "Unfoldings and Bifurcations of Quasi-Periodic Tori," Memoirs Amer. Math. Soc. **83(421)**, 1990.

[3] H.W. Broer and M.B. Sevryuk, *KAM theory: quasi-periodicity in dynamical systems*, preprint.

[4] H.W. Broer and C. Simó, *Hill's equation with quasi-periodic forcing: resonance tongues, instability pockets and global phenomena*, Bol. Soc. Bras. Mat., **29** (1998), 253–293.

[5] H.W. Broer, C. Simó and R. Vitolo, *Bifurcations and strange attractors in the Lorenz-84 climate model with seasonal forcing*, Nonlinearity, **15** (2002), 1205–1267.

[6] H.W. Broer, C. Simó and R. Vitolo. *Quasi-periodic Hénon-like attractors in the Lorenz-84 climate model with seasonal forcing* in "Equadiff 2003, Proceedings International Conference on Differential Equations, Hasselt 2003" (eds. F. Dumortier, H.W. Broer, J. Mahwin, A. Vanderbauwhede and S.M. Verduyn Lunel), World Scientific, (2005), 601–606.

[7] H.W. Broer, C. Simó and R. Vitolo, *Hopf-saddle-node bifurcation for fixed points of 3D-diffeomorphisms: analysis of a resonance 'bubble'*, Physica D, **237** (2008), 1773–1799.

[8] H.W. Broer, C. Simó and R. Vitolo, *The Hopf-saddle-node bifurcation for fixed points of 3D-diffeomorphisms: the Arnol′d resonance web*, Bull. Belgian Math. Soc. Simon Stevin, **15** (2008), 769–787.

[9] H.W. Broer, C. Simó and R. Vitolo, *Chaos and quasi-periodicity in diffeomorphisms of the solid torus*, preprint.

[10] H.W. Broer and F. Takens, "Dynamical Systems and Chaos," Epsilon Uitgaven, Utrecht, 2009.

[11] D.R. Cayan, *Latent and sensible heat flux anomalies over the northern oceans: the connection to monthly atmospheric cirulation*, J. Climate, **5** (1992), 354–369.

[12] F. Chen and M. Ghil, *Interdecadal variability of the thermohaline circulation and high-latitude surface fluxes*, J. Physical Oceanography, **25** (1995), 2547–2568.

[13] A. Chenciner, *Bifurcations de points fixes elliptiques I. Courbes invariantes*, Inst. Hautes Études Sci. Publ. Math., **61** (1985), 67–127.

[14] A. Chenciner, *Bifurcations de points fixes elliptiques II. Orbites péridiques et ensembles de Cantor invariants*, Invent. Math., **80** (1985), 81–106.

[15] A. Chenciner, *Bifurcations de points fixes elliptiques III. Orbites péridiquesde "petites" périodes et élimination résonnante des couples de courbes invariantes*, Inst. Hautes Études Sci. Publ. Math., **66** (1988), 5–91.

[16] A. Colin de Verdière and T. Huck, *Baroclinic instability: an oceanic wavemaker for interdecadal variability*, J. Physical Oceanography, **29** (1999), 893–910.

[17] T.L. Delworth and M.E. Mann, *Observed and simulated multidecadal variability in the Northern Hemisphere*, Climate Dynamics, **16** (2000), 661–676.

[18] H.A. Dijkstra, "Nonlinear Physical Oceanography: a Dynamical Systems Approach to the Large Scale Ocean Circulation and El Niño," 2^{nd} edition, Springer, Dordrecht, 2005.

[19] H.A. Dijkstra, *Interaction of SST modes in the North Atlantic ocean*, J. Physical Oceanography, **36** (2006), 286–299.

[20] H.A. Dijkstra, L.A. te Raa, M. Schmeits and J. Gerrits, *On the physics of the Atlantic Multidecadal Oscillation*, Ocean Dynanmics, **56** (2006), 36–50.

[21] H.A. Dijkstra, L.M. Frankcombe and A.S. von der Heydt, *A stochastic dynamical systems view of the Atlantic Multidecadal Oscillation*, Phil. Trans. R. Soc. A, **366** (2008), 2545–2560.

[22] E.J. Doedel and B.E. Oldeman, *AUTO–07p: continuation and bifurcation software for ordinary differential equations*, Concordia University, Montreal, Canada, 2007.

[23] D. Enfield, A. Mestas-Nuñez and P. Trimble, *The Atlantic multidecadal oscillation and its relation to rainfall and river flows in the continental U.S.*, Geophys. Res. Let., **28** (2001), 2077–2080.

[24] L.M. Frankcombe, H.A. Dijkstra and A.S. von der Heydt, *Noise induced multidecadal variability in the North Atlantic: excitation of normal modes*, J. Physical Oceanography, **39** (2009), 220–233.

[25] S.B. Goldenberg, C.W. Landsea, A.M. Mestas-Nuñez and W.M. Gray, *The recent increase in Atlantic hurricane activity: causes and implications*, Science, **293** (2001), 474–479.

[26] R.J. Greatbatch and S. Zhang, *An interdecadal oscillation in an idealized ocean basin forced by constant heat flux*, J. Climate, **8** (1995), 81–91.

[27] J. Guckenheimer and P. Holmes, "Nonlinear Oscillations, Dynamical Systems and Bifurcations of Vector Fields," Springer, New York, 1983.

[28] T. Huck and G.K. Vallis, *Linear stability analysis of the three-dimensional thermally-driven ocean circulation: application to interdecadal oscillations*, Tellus A, **53** (2001), 526–545.

[29] À. Jorba, *Numerical computation of the normal behaviour of invariant curves of n-dimensional maps*, Nonlinearity, **14** (2001), 943–976.

[30] À. Jorba and M. Zou, *A software package for the numerical integration of ODEs by means of high-order Taylor methods*, Experimental Mathematics, **14** (2005), 99–117.

[31] R.A. Kerr, *A North Atlantic climate pacemaker for the centuries*, Science, **288** (2000), 1984–1985.

[32] Y. Kushnir, *Interdecadal variations in North Atlantic sea surface temperature and associated atmospheric conditions*, J. Climate, **7** (1994), 141–157.

[33] Yu.A. Kuznetsov, "Elements of Applied Bifurcation Theory," 3^{rd} edition, Springer-Verlag, New York, 2004.

[34] F. Kwasniok, *The reduction of complex dynamical systems using principal interaction patterns*, Physica D, **92** (1996), 28–60.

[35] A.I. Neishtadt, C. Simó and D.V. Treschev, *On stability loss delay for a periodic trajectory*, in "Progress in Nonlinear Differential Equations and their Applications," **19**, Birkhäuser-Verlag, (1995), 253–278.

[36] J.C. Robinson, "Infinite-Dimensional Dynamical Systems," Cambridge University Press, Cambridge, 2001.

[37] C. Simó, *On the use of Lyapunov exponents to detect global properties of the dynamics* in "Equadiff 2003, Proceedings International Conference on Differential Equations, Hasselt 2003" (eds. F. Dumortier, H.W. Broer, J. Mahwin, A. Vanderbauwhede and S.M. Verduyn Lunel), World Scientific, (2005), 631–636.

[38] C. Simó, *On the analytical and numerical continuation of invariant manifolds* in "Modern Methods in Celestial Mechanics" (eds. D. Benest and C. Froeschlé), Éditions Frontières, (1990), 285–330.

[39] A.E. Sterk, R. Vitolo, H.W. Broer, C. Simó and H.A. Dijkstra, *New nonlinear mechanisms of midlatitude atmospheric low-frequency variability*, Physica D, **239** (2010), 702–718.

[40] L.A. te Raa and H.A. Dijkstra, *Instability of the thermohaline ocean circulation on interdecadal timescales*, J. Physical Oceanography, **32** (2002), 138–160.

[41] L.A. te Raa and H.A. Dijkstra, *Modes of internal thermohaline variability in a single-hemispheric ocean basin*, J. Marine Res., **61** (2003), 491–516.

[42] L.A. te Raa, J. Gerrits and H.A. Dijkstra, *Identification of the mechanisms of interdecadal variability in the North Atlantic Ocean*, J. Physical Oceanography, **34** (2004), 2792–2807.

[43] R. Temam, "Infinite-Dimensional Dynamical Systems in Mechanics and Physics," 2^{nd} edition, Springer-Verlag, New York, 1997.

[44] P.C.F. van der Vaart, H.M. Schuttelaars, D. Calvete and H.A. Dijkstra, *Instability of time-dependent wind-driven ocean gyres*, Phys. Fluids, **14** (2002), 3601–3615.

[45] R. Vitolo, H.W. Broer and C. Simó, *Routes to chaos in the Hopf-saddle-node bifurcation for fixed points of 3D-diffeomorphisms*, preprint.

Received xxxx 20xx; revised xxxx 20xx.

E-mail address: `h.w.broer@rug.nl`
E-mail address: `h.a.dijkstra@uu.nl`
E-mail address: `carles@maia.ub.es`
E-mail address: `a.e.sterk@rug.nl`
E-mail address: `r.vitolo@exeter.ac.uk`